Self-Similarity of Time-Evolving Plane Wakes

By ROBERT D. MOSER,[1] MICHAEL M. ROGERS[2] AND DANIEL W. EWING[3]

[1]Department of Theoretical and Applied Mechanics, University of Illinois, Urbana, IL 61801, USA

[2]NASA-Ames Research Center, Moffett Field, CA 94035, USA

[3]Department of Mechanical Engineering, Queens University, Kingston, Ontario K7L 3N6, Canada

(Received 25 July 1996)

Direct numerical simulations of three time-developing turbulent plane wakes have been performed. Initial conditions for the simulations were obtained from two realizations of a direct simulation of a turbulent boundary layer at momentum thickness Reynolds number 670. In addition, extra two-dimensional disturbances were added in two of the cases to mimic two-dimensional forcing. The wakes are allowed to evolve long enough to attain self-similarity, although in the strongly forced case this self-similarity is only approximate and of short duration. For all three flows, the mass-flux Reynolds number (equivalent to the momentum thickness Reynolds number in spatially developing wakes) is 2000, which is high enough for a short $k^{-5/3}$ range to be evident in the streamwise one-dimensional velocity spectrum.

The spreading rate, turbulence Reynolds number, and turbulence intensities all increase with forcing (by nearly an order of magnitude for the strongly forced case), with experimental data falling between the unforced and weakly forced cases. The simulation results are used in conjunction with a complete self-similar analysis of the Reynolds stress equations to develop scalings that approximately collapse the profiles from different wakes. Factors containing the wake spreading rate are required to bring profiles from different wakes into agreement. Part of the difference between the various cases is due to the increased level of spanwise coherent (roughly two-dimensional) energy in the forced cases. Forcing also has a significant impact on flow structure, with the forced flows exhibiting more organized large-scale structures similar to those observed in transitional wakes.

1. Introduction

The plane wake studied here is one of several canonical free-shear flows that is used as a test flow for the development of turbulence models and turbulence control strategies. These flows are also of interest in many practical engineering applications; for example, high-lift airfoil configurations where one lifting surface (a flap) may operate in or near the wake of an upstream component. The numerical simulations reported here are the first of several to be performed to provide data for turbulence modeling relevant to such a configuration.

The evolution of the wake is generally broken up into three regions; the near field, an intermediate field, and the far or "equilibrium" region of the wake. It is widely recognized

that the dynamics of the large-scale coherent structures in the flow play a dominant role in the first two regions of the flow; however, their role in the latter region is not as well known. It is also known that in this latter region the governing equations for the single-point moments admit similarity solutions in the small-deficit (or infinite downstream distance, x) limit, where the thickness of the layer grows as $x^{1/2}$. Traditionally, it was argued (*e.g.* Townsend 1976) that the effect of differences in the initial conditions (that produce differences in the near field) die out, so that the asymptotic state of all wakes is universal. This hypothesis was not supported by later experimental evidence. For example, Wygnanski, Champagne & Marasli (1986) reported wake growth rates of between 0.29 and 0.41 depending on the body used to generate the flow. Even larger growth rates could be achieved if two-dimensional forcing was used to excite the large-scale motions (Wygnanski *et al.* 1986; Marasli, Champagne & Wygnanski 1992). The profiles of the scaled turbulent normal stresses in the wake far-field were also different, despite the collapse of the mean velocity profiles as predicted in a similarity analysis by George (1989).

The evolution of large-scale coherent structures in the plane wake has been of great interest (e.g. Antonia, Browne & Bisset 1987; Hayakawa & Hussain 1989). Part of the reason for this interest is that the well-known features of transitional wakes, such as the Karman street, have been observed in the turbulent wake as well. George (1989) argued that the differences between the asymptotic states in the far field of the wake were due to the persistence of different large-scale structures from the near field into the far field of the wake. However, the extent to which such structures are dynamically important in the far field and how they vary among different wakes is not, as yet, well understood. For example, the level of the "two dimensionality" that occurs in developed free-shear flows has been widely debated, with some researchers claiming that the relatively organized large-scale structures will ultimately break down into more three-dimensional turbulence. It is thus of interest to determine if wakes can achieve self-similar states with different flow structures. To this end, a complimentary study was also carried out to examine if the governing equations for more complex statistical measures of the turbulent structures (in particular the two-point velocity correlation) admit similarity solutions.

The "apparent" non-uniqueness of the asymptotic states provides both complications and opportunities. It complicates the prediction of the flow using turbulence models since it is necessary to ensure that the model allows for multiple asymptotic states. The non-uniqueness of the flow, though, suggests that it should be possible to control the evolution of the wake by manipulation of the generating body. Progress in both of these areas will be facilitated by knowledge of how the differences in the statistical measures and structures the far wake are related to differences in the initial state of the wake. Direct numerical simulation is an ideal tool for providing this information because it allows the precise prescription of the intial/inlet conditions and also provides very detailed information about the flow. Three such simulations with differing initial conditions are reported here. The results of the simulations are used in conjunction with a similarity analysis following the approach outlined by George (1989) to examine the differences between the "equilibrium" states of the three flows. The simulations are described in section §2, details of the self-similar analysis and statistical descriptions of the three simulated flows are presented in §3, and the structural features of the flows are discussed in §4. Finally, some concluding remarks are given in §5.

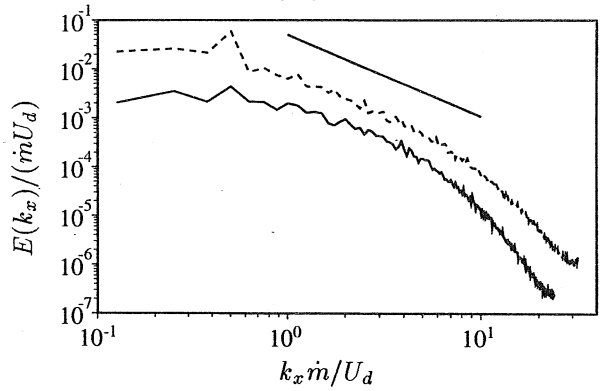

FIGURE 1. Streamwise one-dimensional energy spectra at the wake centerline $y = 0$ in the ——— unforced wake simulation at $\tau = tU_d^2/\dot{m} = 91.5$ and - - - - the strongly forced wake simulation at $\tau = tU_d^2/\dot{m} = 50.0$. The straight line shows a $k^{-5/3}$ dependence.

2. The Simulations

The numerical simulations discussed here were performed by directly solving the three-dimensional time-dependent incompressible Navier–Stokes equations with a Galerkin spectral method (Spalart, Moser & Rogers 1991). For computational efficiency, a temporally evolving plane wake was simulated rather than the spatially evolving flow typical of experiments. The spatially and temporally evolving wakes differ in that different integral quantities are preserved. In the time-developing wake, the cross-stream integrated mass flux deficit (normalized by density and unit depth) $\dot{m} = -\int_{-\infty}^{\infty} \delta U \, dy$ is preserved (the velocity deficit is $\delta U = \overline{U} - U_\infty$, where $\overline{U}$ and U_∞ are the mean and free-stream velocities, respectively), while in the spatially evolving wake, the integrated momentum flux deficit $U_\infty^2\theta = -\int_{-\infty}^{\infty} \delta U(U_\infty + \delta U)\, dy$ is preserved. In the limit of small deficits, the temporally evolving wake is equivalent to a spatially evolving wake viewed in a frame moving with the free stream, and in this limit, the mass flux deficit is given by $\dot{m} = U_\infty\theta$. In the incompressible time-developing wake, the free-stream velocity is irrelevant, only the deficit is important. Thus, in what follows, nondimensionalization will be based on $\dot{m}$ and the initial magnitude of the velocity deficit, U_d. In the three flows described here, the Reynolds number $Re_m = \dot{m}/\nu$ is 2000. This Reynolds number is high enough to produce a short $k^{-5/3}$ spectral range in the streamwise one-dimensional spectrum (figure 1).

The initial conditions for this study were generated using two realizations of a turbulent boundary layer with a momentum thickness Reynolds number of 670, as computed by Spalart (1988). The solution domain for the simulations is periodic in the streamwise (x) and spanwise (z) directions with periods $50\dot{m}/U_d$ and $12.5\dot{m}/U_d$, respectively, to correspond to those in the boundary layer simulations. Different realizations were used for each side of the wake to avoid any false instantaneous symmetries, and the free-stream velocity on each side was zero. Thus, the simulations represent a temporally evolving approximation to the wake behind a zero-thickness flat plate at zero angle of attack moving at velocity U_d with turbulent boundary layers. In order to mimic the expected receptivity of the trailing edge of the plate to two-dimensional disturbances, two of the three simulations included extra two-dimensional forcing in the initial conditions. To model the uncontrolled nature of these two-dimensional disturbances in a flat-plate wake, the forcing was introduced by amplifying the streamwise and cross-stream components (u and v) of all the two-dimensional modes in the boundary layer initial condition. These motions were amplified by a factor of 5 in one case and a factor of 20 in the

other. The flows studied here will thus be referred to as the unforced, weakly forced, and strongly forced wakes. The forcing level in the strongly forced flow is large, with the two-dimensional amplification increasing the total initial disturbance energy by a factor of 13 and adding energy of $0.7\dot{m}U_d$ per unit plan area to the flow. In similar simulations of a mixing layer (Rogers & Moser 1994), the amplification factor of 20 was needed to produce a significant effect. The wakes examined here are apparently more sensitive to forcing (perhaps because the shear production of turbulence in the wake decreases significantly compared to that in the mixing layer as the wake velocity deficit decays), and even the "weak" forcing was found to markedly effect the wake.

To achieve the relatively large Reynolds numbers of the computations, while at the same time maintaining an adequate sample of large-scale eddies in the computational domain, requires significant computational resources. The simulations described here employed grids with up to 25 million modes ($600 \times 260 \times 160$) and required between 220 and 530 Cray YMP C-90 CPU hours each to complete.

3. Self-similarity and Statistics

3.1. *Similarity of single-point velocity moments*

The temporally evolving plane wake is statistically homogeneous in both the streamwise and the spanwise directions (*i.e.*, x and z directions), so the mean momentum equation in deficit form is given by

$$\frac{\partial \delta U}{\partial t} = -\frac{\partial \overline{uv}}{\partial y} + \nu \frac{\partial^2 \delta U}{\partial y^2} \tag{3.1}$$

where u and v are the streamwise (x) and cross-stream (y) velocity fluctuations respectively, and an overbar signifies expected value or average. Since the self-similar wake evolves at constant Reynolds number, the viscous term can be retained in this analysis, unlike in the conventional approach (*c.f.*, Tennekes & Lumley 1972) in which it is neglected. A high-Reynolds-number assumption is thus avoided. By integrating (3.1) across the layer, and assuming zero free-stream turbulence, it is confirmed that

$$\int_{-\infty}^{\infty} \delta U \, dy = -\dot{m}, \tag{3.2}$$

is a constant.

It is hypothesized that the mean momentum equations (3.1) and (3.2) for this flow admit similarity solutions where the mean velocity profile and the Reynolds stress are given by

$$\delta U = U_s(t) f(\eta) \tag{3.3}$$

and

$$\overline{uv} = R_s(t) g(\eta), \tag{3.4}$$

where $\eta = y/\delta(t)$ is the similarity coordinate. Here we follow the technique of George (1989), choosing individual scales for each of the moments to avoid the possibility of over-constraining the analysis. In particular, it is not assumed *a priori* that the scale for the Reynolds stress $\overline{uv}$ is U_s^2. This scale is determined instead by the constraints imposed by the equations of motion.

Substituting the hypothesized similarity solutions into equations (3.1) and (3.2) yields

$$\left[\frac{dU_s}{dt}\right] f - \left[\frac{U_s}{\delta}\frac{d\delta}{dt}\right] \eta \frac{df}{d\eta} = -\left[\frac{R_s}{\delta}\right] \frac{dg}{d\eta} + \nu \left[\frac{U_s}{\delta^2}\right] \frac{d^2 f}{d\eta^2} \tag{3.5}$$

and

$$[U_s\delta]\int_{-\infty}^{\infty} f(\eta)d\eta = -\dot{m}. \tag{3.6}$$

The time dependent portion of each term in (3.5) and (3.6) is contained in square brackets (a convention that will be used throughout this similarity analysis). Thus, the hypothesized similarity solutions are consistent with the mean momentum equations if

$$[U_s\delta] \propto \dot{m} \tag{3.7}$$

and

$$\left[\frac{dU_s}{dt}\right] \propto \left[\frac{U_s}{\delta}\frac{d\delta}{dt}\right] \propto \left[\frac{R_s}{\delta}\right] \propto \left[\frac{U_s}{\delta^2}\right], \tag{3.8}$$

assuming, of course, that none of these terms are zero or negligible. It is straightforward to demonstrate that these constraints are only satisfied when

$$U_s \propto \frac{1}{\delta}, \tag{3.9}$$

$$\frac{d\delta^2}{dt} = \text{constant}, \tag{3.10}$$

and

$$R_s \propto U_s\frac{d\delta}{dt}. \tag{3.11}$$

Thus, when the flow evolves in a manner consistent with a similarity solution, it follows that

$$\delta \propto (t-t_o)^{1/2}, \quad U_s \propto (t-t_o)^{-1/2}, \quad \text{and} \quad R_s \propto (t-t_o)^{-1}, \tag{3.12}$$

where t_o is some virtual origin.

Following the methodology outlined by George (1994), the similarity analysis can also be applied to the equations governing the evolution of the individual Reynolds stress components. The transport equations for Reynolds stress components in the temporally evolving plane wake are given by

$$\frac{\partial\overline{u^2}}{\partial t} = -2\overline{uv}\frac{\partial\delta U}{\partial y} - \frac{\partial\overline{u^2v}}{\partial y} + 2\overline{\frac{p}{\rho}\frac{\partial u}{\partial x}} + \nu\frac{\partial^2\overline{u^2}}{\partial y^2} - \epsilon_{uu}, \tag{3.13a}$$

$$\frac{\partial\overline{v^2}}{\partial t} = -\frac{\partial\overline{v^3}}{\partial y} + 2\overline{\frac{p}{\rho}\frac{\partial v}{\partial y}} - \frac{2}{\rho}\frac{\partial\overline{pv}}{\partial y} + \nu\frac{\partial^2\overline{v^2}}{\partial y^2} - \epsilon_{vv}, \tag{3.13b}$$

$$\frac{\partial\overline{w^2}}{\partial t} = -\frac{\partial\overline{w^2v}}{\partial y} + 2\overline{\frac{p}{\rho}\frac{\partial w}{\partial z}} + \nu\frac{\partial^2\overline{w^2}}{\partial y^2} - \epsilon_{ww}, \tag{3.13c}$$

and

$$\frac{\partial\overline{uv}}{\partial t} = -\overline{v^2}\frac{\partial\delta U}{\partial y} - \frac{\partial\overline{uv^2}}{\partial y} + \overline{\frac{p}{\rho}\left(\frac{\partial u}{\partial y}+\frac{\partial v}{\partial x}\right)} - \frac{1}{\rho}\frac{\partial\overline{pu}}{\partial y} + \nu\frac{\partial^2\overline{uv}}{\partial y^2} - \epsilon_{uv}, \tag{3.13d}$$

where p is the fluctuating pressure, ρ is the density, and ϵ_{ij} are the dissipation-rate terms $2\nu\overline{\frac{\partial u_i}{\partial x_l}\frac{\partial u_j}{\partial x_l}}$. For example, ϵ_{uu} is given by

$$\epsilon_{uu} = 2\nu\left\{\overline{\left(\frac{\partial u}{\partial x}\right)^2} + \overline{\left(\frac{\partial u}{\partial y}\right)^2} + \overline{\left(\frac{\partial u}{\partial z}\right)^2}\right\}. \tag{3.14}$$

Finally, due to incompressibility, the pressure-strain terms in the normal stress equations

must sum to zero

$$\overline{\frac{p}{\rho}\frac{\partial u}{\partial x}} + \overline{\frac{p}{\rho}\frac{\partial v}{\partial y}} + \overline{\frac{p}{\rho}\frac{\partial w}{\partial z}} = 0. \tag{3.15}$$

As was done for the mean equation, it is hypothesized that similarity solutions exist for the new moments in the Reynolds stress equations. For example, in the $\overline{u^2}$ equation the solutions are

$$\overline{u^2} = K_u(t)k_u(\eta), \tag{3.16a}$$

$$\overline{u^2 v} = Tt_u(t)tt_u(\eta), \tag{3.16b}$$

$$\overline{\frac{p}{\rho}\frac{\partial u}{\partial x}} = \Pi_u(t)\pi_u(\eta), \tag{3.16c}$$

and

$$\epsilon_{uu} = D_u(t)d_u(\eta). \tag{3.16d}$$

The assumed solutions for the other terms in the equations are given in the second column of table 1.

Substituting the hypothesized forms of the similarity solutions (and those defined previously) into (3.13) yields

$$\left[\frac{dK_u}{dt}\right] k_u - \left[\frac{K_u}{\delta}\frac{d\delta}{dt}\right] \eta\frac{dk_u}{d\eta} = -2\left[\frac{R_s U_s}{\delta}\right] g\frac{df}{d\eta} - \left[\frac{Tt_u}{\delta}\right]\frac{dtt_u}{d\eta} + 2\left[\Pi_u\right]\pi_u + \nu\left[\frac{K_u}{\delta^2}\right]\frac{d^2k_u}{d\eta^2} - \left[D_u\right]d_u\,, \tag{3.17}$$

where again the time-dependent portion of each term is contained in square brackets. The other equations are analogous. If the time-dependence of the coefficients in brackets are identical, then the equations admit similarity solutions of the form given in table 1. Thus for a similarity solution, it is sufficient that

$$\left[\frac{dK_u}{dt}\right] \propto \left[\frac{K_u}{\delta}\frac{d\delta}{dt}\right] \propto \left[\frac{R_s U_s}{\delta}\right] \propto \left[\frac{Tt_u}{\delta}\right] \propto \left[\Pi_u\right] \propto \left[\frac{K_u}{\delta^2}\right] \propto \left[D_u\right] \tag{3.18a}$$

$$\left[\frac{dK_v}{dt}\right] \propto \left[\frac{K_v}{\delta}\frac{d\delta}{dt}\right] \propto \left[\frac{Tt_v}{\delta}\right] \propto \left[\Pi_v\right] \propto \left[\frac{Pt_v}{\delta}\right] \propto \left[\frac{K_v}{\delta^2}\right] \propto \left[D_v\right], \tag{3.18b}$$

$$\left[\frac{dK_w}{dt}\right] \propto \left[\frac{K_w}{\delta}\frac{d\delta}{dt}\right] \propto \left[\frac{Tt_w}{\delta}\right] \propto \left[\Pi_w\right] \propto \left[\frac{K_w}{\delta^2}\right] \propto \left[D_w\right], \tag{3.18c}$$

$$\left[\frac{dR_s}{dt}\right] \propto \left[\frac{R_s}{\delta}\frac{d\delta}{dt}\right] \propto \left[\frac{K_v U_s}{\delta}\right] \propto \left[\frac{Tt_{uv}}{\delta}\right] \propto \left[\Pi_{uv}\right] \propto \left[\frac{Pt_{uv}}{\delta}\right] \propto \left[\frac{R_s}{\delta^2}\right] \propto \left[D_{uv}\right], \tag{3.18d}$$

and

$$\left[\Pi_u\right] \propto \left[\Pi_v\right] \propto \left[\Pi_w\right], \tag{3.18e}$$

where the last condition arises from the requirement that the pressure strain terms sum to zero (3.15). Although the conditions (3.18*a*)–(3.18*e*) are sufficient for self-similarity they are not necessary. In theory, groups of terms in the equations could balance and scale independently. However, without any further physical insight as to why this might happen (and for which groups of terms), these solutions could only be found using empirical techniques.

It is clear that the constraints in (3.18*a*) are satisfied if the scales for the terms in the

Term	Form	Similarity Conditions	Scaling for (3.25)–(3.25)
δU	$U_s(t)f(\eta)$	$U_s \propto \frac{1}{\delta}$	
$\overline{u^2}$	$K_u(t)k_u(\eta)$	$K_u \propto U_s^2$	$K_u = U_s^2\beta$
$\overline{v^2}$	$K_v(t)k_v(\eta)$	$K_v \propto U_s^2$	$K_v = U_s^2\beta^2$
$\overline{w^2}$	$K_w(t)k_w(\eta)$	$K_w \propto U_s^2$	$K_w = U_s^2\beta$
$\overline{uv}$	$R_s(t)g(\eta)$	$R_s \propto U_s\frac{d\delta}{dt}$	$R_s = U_s^2\beta$
$\overline{\frac{p}{\rho}\frac{\partial u}{\partial x}}$	$\Pi_u(t)\pi_u(\eta)$	$\Pi_u \propto \frac{U_s^2}{\delta}\frac{d\delta}{dt}$	$\Pi_u = \frac{U_s^3\beta^2}{\delta}$
$\overline{\frac{p}{\rho}\frac{\partial v}{\partial y}}$	$\Pi_v(t)\pi_v(\eta)$	$\Pi_v \propto \frac{U_s^2}{\delta}\frac{d\delta}{dt}$	$\Pi_v = \frac{U_s^3\beta^2}{\delta}$
$\overline{\frac{p}{\rho}\frac{\partial w}{\partial z}}$	$\Pi_w(t)\pi_w(\eta)$	$\Pi_w \propto \frac{U_s^2}{\delta}\frac{d\delta}{dt}$	$\Pi_w = \frac{U_s^3\beta^2}{\delta}$
$\overline{\frac{p}{\rho}\left(\frac{\partial u}{\partial y}+\frac{\partial v}{\partial x}\right)}$	$\Pi_{uv}(t)\pi_{uv}(\eta)$	$\Pi_{uv} \propto \frac{U_s}{\delta}\left(\frac{d\delta}{dt}\right)^2$	$\Pi_{uv} = \frac{U_s^3\beta^2}{\delta}$
$\overline{u^2v}$	$Tt_u(t)tt_u(\eta)$	$Tt_u \propto U_s^2\frac{d\delta}{dt}$	$Tt_u = U_s^3\beta^2$
$\overline{v^3}$	$Tt_v(t)tt_v(\eta)$	$Tt_v \propto U_s^2\frac{d\delta}{dt}$	$Tt_v = U_s^3\beta^3$
$\overline{w^2v}$	$Tt_w(t)tt_w(\eta)$	$Tt_w \propto U_s^2\frac{d\delta}{dt}$	$Tt_w = U_s^3\beta^2$
$\overline{uv^2}$	$Tt_{uv}(t)tt_{uv}(\eta)$	$Tt_{uv} \propto U_s\left(\frac{d\delta}{dt}\right)^2$	$Tt_{uv} = U_s^3\beta^2$
$\overline{\frac{pv}{\rho}}$	$Pt_v(t)pt_v(\eta)$	$Pt_v \propto U_s^2\frac{d\delta}{dt}$	$Pt_v = U_s^3\beta^3$
$\overline{\frac{pu}{\rho}}$	$Pt_{uv}(t)pt_{uv}(\eta)$	$Pt_{uv} \propto U_s\left(\frac{d\delta}{dt}\right)^2$	$Pt_{uv} = U_s^3\beta^3$
ϵ_{uu}	$D_u(t)d_u(\eta)$	$D_u \propto \frac{U_s^2}{\delta}\frac{d\delta}{dt}$	$D_u = \frac{U_s^3\beta^2}{\delta}$
ϵ_{vv}	$D_v(t)d_v(\eta)$	$D_v \propto \frac{U_s^2}{\delta}\frac{d\delta}{dt}$	$D_v = \frac{U_s^3\beta^2}{\delta}$
ϵ_{ww}	$D_w(t)d_w(\eta)$	$D_w \propto \frac{U_s^2}{\delta}\frac{d\delta}{dt}$	$D_w = \frac{U_s^3\beta^2}{\delta}$
ϵ_{uv}	$D_{uv}(t)d_{uv}(\eta)$	$D_{uv} \propto \frac{U_s^2}{\delta}\frac{d\delta}{dt}$	$D_{uv} = \frac{U_s^3\beta}{\delta}$

TABLE 1. Similarity forms for terms in the mean and Reynolds stress equations

normal stress $\overline{u^2}$ equation are chosen such that

$$K_u \propto U_s^2, \tag{3.19}$$

$$Tt_u \propto U_s^2 \frac{d\delta}{dt}, \tag{3.20}$$

and

$$\Pi_u \propto D_u \propto \frac{U_s^2}{\delta}\frac{d\delta}{dt}. \tag{3.21}$$

Similarly, the other Reynolds stress transport equations admit self-similar solutions when the scales are given as in the third column of table 1. Note that the similarity conditions for the Reynolds shear stress equation (3.18*d*) and the scalings in table 1 require that

$$\left[\frac{R_s}{\delta}\frac{d\delta}{dt}\right] \propto \left[\frac{K_v U_s}{\delta}\right] \Rightarrow \left(\frac{d\delta}{dt}\right)^2 \propto U_s^2, \tag{3.22}$$

which using (3.9) implies that

$$\frac{d\delta^2}{dt} = \text{constant}, \tag{3.23}$$

in agreement with the result from the analysis of the mean momentum equation (3.10). It is comforting that the self-similar growth behavior of the layer is not determined solely by the viscous term in the mean equation, which is arguably negligible for high-Reynolds-number wakes.

The similarity requirements outlined above only require that the time-dependent portions of the solutions are proportional to the given scales. As George (1989) argued, the value of these constants of proportionality may depend on the initial (or source) conditions of the flow. This dependence is expressed in terms of a number of non-dimensional constants. The most important, in this case, is the ratio of the two different velocity scales used in the analysis: U_s, a convective velocity scale, and $d\delta/dt$, a characteristic velocity scale for the growth rate of the layer. This ratio

$$\beta = \frac{1}{U_s}\frac{d\delta}{dt} = \frac{1}{2U_s\delta}\frac{d\delta^2}{dt} = -\frac{\delta}{U_s^2}\frac{dU_s}{dt} \tag{3.24}$$

is a constant in a self-similar wake from (3.9) and (3.23) and is a nondimensional measure of the growth rate of the layer. Note that this ratio can also be interpreted as the ratio of a convective time scale and a time scale characteristic of the spreading rate of the flow. This interpretation is useful in the analysis of the moments involving velocities at two times that will be discussed elsewhere.

For example, using the scaling in the fourth column of table 1, the resulting governing equations for the similarity profiles are given by:

$$\int_{-\infty}^{\infty} f(\eta)d\eta = \frac{-\dot{m}}{U_s\delta}, \tag{3.25a}$$

$$-\frac{d\eta f}{d\eta} = -\frac{dg}{d\eta} + \frac{1}{Re_\delta\beta}\frac{d^2 f}{d\eta^2}, \tag{3.25b}$$

$$-2k_u - \eta\frac{dk_u}{d\eta} = -\left\{\frac{1}{\beta}\right\} 2g\frac{df}{d\eta} - \frac{dtt_u}{d\eta} + 2\pi_u + \frac{1}{Re_\delta\beta}\frac{d^2 k_u}{d\eta^2} - d_u, \tag{3.25c}$$

$$-2k_v - \eta\frac{dk_v}{d\eta} = -\frac{dtt_v}{d\eta} + \left\{\frac{1}{\beta}\right\} 2\pi_v - 2\frac{dpt_v}{d\eta} + \frac{1}{Re_\delta\beta}\frac{d^2 k_v}{d\eta^2} - \left\{\frac{1}{\beta}\right\} d_v, \tag{3.25d}$$

$$-2k_w - \eta\frac{dk_w}{d\eta} = -\frac{dtt_w}{d\eta} + 2\pi_w + \frac{1}{Re_\delta\beta}\frac{d^2k_w}{d\eta^2} - d_w, \tag{3.25e}$$

$$-2g - \eta\frac{dg}{d\eta} = -k_v\frac{df}{d\eta} - \frac{dtt_{uv}}{d\eta} + \pi_{uv} - \{\beta\}\frac{dpt_{uv}}{d\eta} + \frac{1}{Re_\delta\beta}\frac{d^2g}{d\eta^2} - \left\{\frac{1}{\beta}\right\}d_{uv} \tag{3.25f}$$

and

$$\pi_u + \pi_v + \pi_w = 0, \tag{3.25g}$$

where $Re_\delta = U_s\delta/\nu$ is the Reynolds number. Note that these equations depend on three parameters. One of these ($\dot{m}/U_s\delta$) only reflects the normalization chosen for the mean velocity, and is of no dynamic significance. The other two are the Reynolds number and β. By switching to the Reynolds number based on the velocity scale $d\delta/dt$ the dependence on the growth rate β can be removed from the viscous terms. If a scaling could be chosen that would eliminate all the β-dependent coefficients in the profile equations, then the plane wake would admit a family of self-similar states with different growth rates but identical similarity profiles (when properly scaled). However, in this case it is not possible to remove the β coefficients from all of the terms in the stress equations or the pressure-strain balance regardless of what factors of β are chosen for the individual scales. Furthermore, although the growth rate dependence may only appear in one or a few of the equations, the equations are coupled so the growth-rate dependence can affect all the profiles. As a result, the shape of the similarity profiles for the single-point moments must differ for wakes with different normalized growth rates.

The most appropriate choice for the scale factors can be found by examining the equations of motion or data from different wakes. Such wakes *necessarily* have different self-similar profiles, but certain scalings may be able to minimize the differences in overall magnitude of the profiles. The particular scalings given in the fourth column of table 1 were selected with guidance from the DNS data (§3.2) and represent the scalings that minimize the gross magnitude variations among the profiles for wakes with different growth rates. Use of these scalings results in more factors of β in the profile equations than the minimum possible.

Note that scaling the Reynolds shear stress with $U_s^2\beta$ has resulted in a mean velocity equation (3.25) without explicit growth rate dependence. Thus, if wakes with different growth rates have universal mean velocity profiles as is observed both in experiments (Wygnanski *et al.* 1986) and the current numerical simulations (§3.2), then the Reynolds stress profile scaled in this way must also be universal. Indeed, this was the major motivation in scaling $\overline{uv}$ with $U_s^2\beta$. Similarly, by scaling $\overline{v^2}$ with $U_s^2\beta^2$, the production term in the $\overline{uv}$ equation (3.25) appears with no explicit growth rate dependence. A shear-stress equation with no β factors can be produced by different choices from those in table 1 for the pressure transport and dissipation terms. This, together with the universality of $\overline{uv}$, means that the $\overline{v^2}$ profile (k_v) could also be universal. The scaling chosen in table 1 (based on the simulation results) implies that this is not the case. The $\overline{uv}$ equation involves the sum of several different terms, which individually may not be universal although their sum is.

It is evident from the above analysis that the governing equations for the Reynolds stresses in the time-developing wake admit similarity solutions. Of course, this analysis only confirms that the solutions are possible and does not imply that they must occur in reality. Further, the analysis assumes that self-similar solutions exist for various higher-order quantities (e.g. the pressure-strain terms, the transport terms, and the dissipation). It is not possible to verify this analytically because of the closure problem; the single-point moments do not include the necessary non-local information to evaluate them. Thus in order to determine if the hypothesized solutions are a good description of an

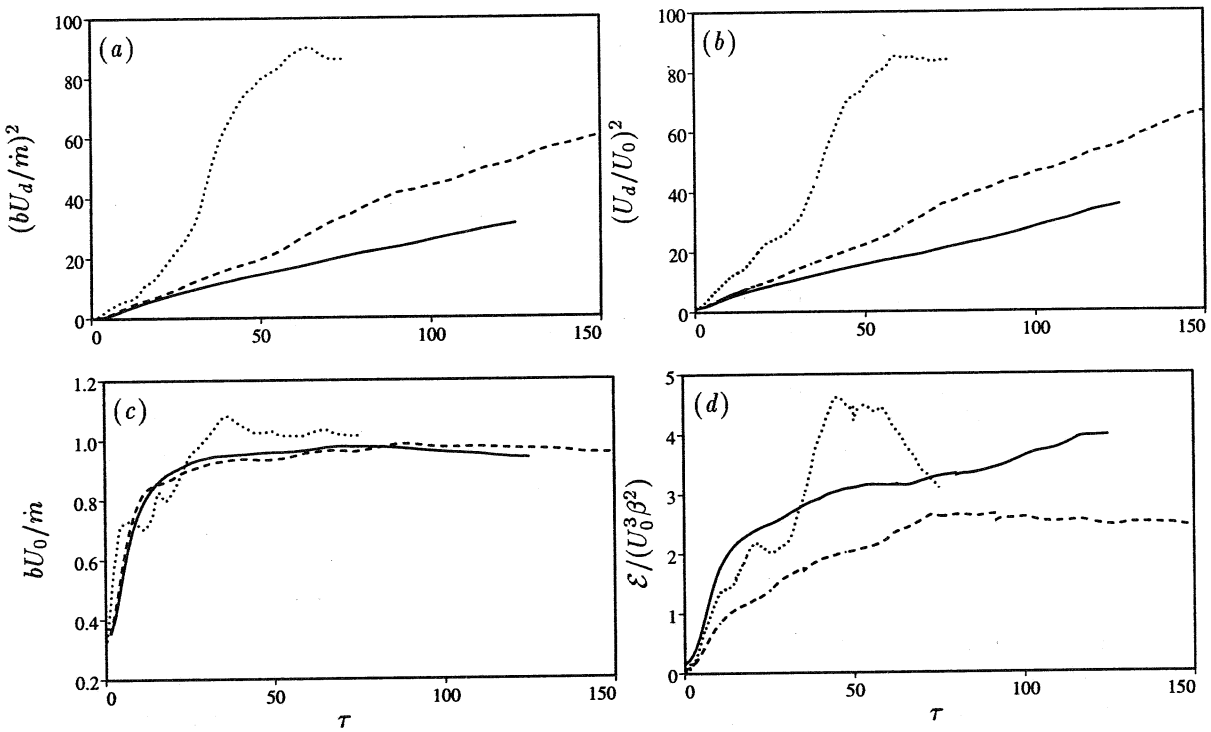

FIGURE 2. Evolution of (a) $(bU_d/\dot{m})^2$, (b) $(U_d/U_0)^2$, (c) $bU_0/\dot{m}$, and (d) $\mathcal{E}/(U_0^3\beta^2)$ in the ——— unforced, - - - - weakly forced, and ····· strongly forced wake simulations.

actual flow it is necessary to test the predictions of the theory with experimental or simulated flow data.

3.2. *Comparison with the simulations*

In this section, the simulations described in §2 are examined to determine whether the similarity described in §3.1 is achieved. Formally the time-developing plane wake can only be self-similar if the streamwise and spanwise domain sizes are infinite. Otherwise, the finite domain size would introduce a physical length scale (other than a characteristic wake thickness), which results in a loss of self-similarity. Of course the simulations performed here have finite streamwise and spanwise domain sizes, which means that if self-similarity is to be achieved, the domain size must be much larger than the largest scales of the turbulence, so that the evolution of the turbulence will not be affected by the finite domain. As the size of the turbulent eddies grows in time, the infinite-domain approximation breaks down and results in the loss of similarity at late times in the simulations. During the self-similar period of the simulations, the finite-domain simulation is used as an approximation of the infinite-domain self-similar wake.

In applying the similarity analysis to the simulated wakes, any number of different thickness measures (δ) and velocity scales (U_s) could be used. To facilitate comparison to previous experimental data, we will use the maximum magnitude of the velocity deficit (U_0) and the half-width b, which is defined to be the distance between the y-locations at which the mean velocity is half of U_0 (note that some investigators take the half-width to be half this distance).

Shown in figure 2 are the time evolutions of b^2 and U_0^{-2} for all three simulations plotted against the dimensionless time $\tau = tU_d^2/\dot{m}$. Both these quantities should evolve linearly

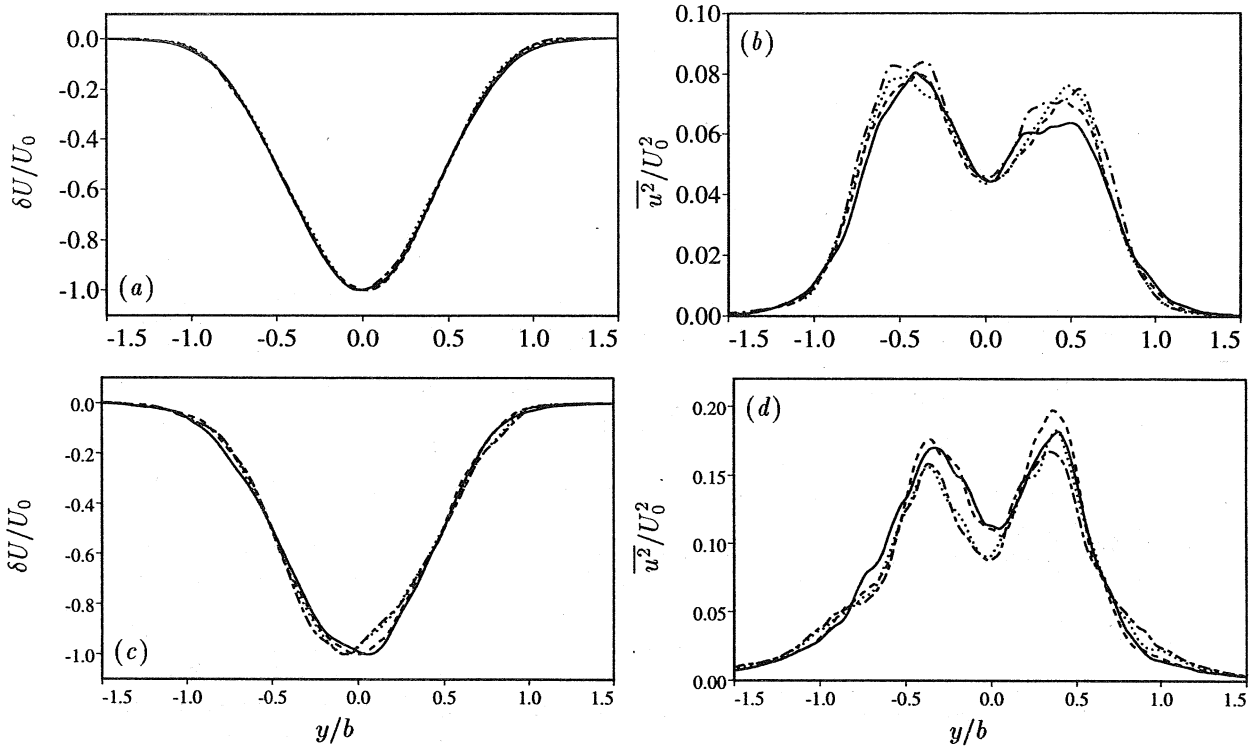

FIGURE 3. Collapse of $\delta U/U_0$ in the (a) unforced and (c) weakly forced wakes, and $\overline{u^2}/U_0^2$ in the (b) unforced and (d) weakly forced wakes, in scaled coordinates at four times during the self-similar period. Profiles from the unforced and weakly forced wakes were taken at at ——— $\tau = 42.8$ and 64.6, - - - - $\tau = 56.6$ and 83.1, ····· $\tau = 71.7$ and 105.6, and —·— $\tau = 91.5$ and 120.9, respectively.

during self-similarity as required by (3.9) and (3.10), and indeed in the unforced and weakly forced flows both have substantial periods of linear growth. The growth rate can be characterized by the nondimensional growth, β (see §3.1), which when based on U_0 and b is given by

$$\beta = \frac{1}{U_0}\frac{db}{dt}\,, \tag{3.26}$$

In the unforced and weakly forced flows $\beta = 0.12$ and 0.21, respectively. The analogous growth rate parameter in a spatially developing wake is $\beta = \frac{U_\infty}{U_0}\frac{db}{dx}$ which was 0.18 in the experiments of Weygandt & Mehta (1993) and ranged from 0.15 to 0.21 in the experiments of Wygnanski *et al.* (1986). Thus the unforced and weakly forced growth rates cover the range of these experimental growth rates. In contrast, the strongly forced case has no extended period of self-similar growth, although there are short periods during which b^2 and/or U_0^{-2} vary linearly. The period that most closely approaches self-similarity in the strongly forced case occurs from about $\tau = 40$ to $\tau = 58$. Here bU_0 (figure 2(c)) appears to be reaching a plateau, indicating that b and U_0 are evolving together ($\beta = 0.58$ at this time in the strongly forced flow). Furthermore the statistical profiles discussed below are roughly consistent with self-similarity during this time interval.

Another global quantity that can be examined for evidence of self-similarity is

$$\mathcal{E} = \int_{-\infty}^{\infty} \epsilon \, dy = \int_{-\infty}^{\infty} \frac{1}{2}(\epsilon_{uu} + \epsilon_{vv} + \epsilon_{ww}) \, dy \, , \tag{3.27}$$

the integrated rate of kinetic energy dissipation ($\epsilon = 2\nu\overline{S_{ij}S_{ij}}$, where S_{ij} is the strain-rate tensor and ν is the kinematic viscosity). Note that because the flow is inhomogeneous in y $\epsilon \neq \epsilon_{uu} + \epsilon_{vv} + \epsilon_{ww}$. However, the integral relation in equation (3.27) does hold. According to the scaling in table 1, the integrated dissipation rate should scale with $U_0^3\beta^2$. Thus $\mathcal{E}/(U_0^3\beta^2)$ should be a constant during self-similarity. In figure 2(d), it is shown that $\mathcal{E}/(U_0^3\beta^2)$ is indeed approximately constant for $40 \leq \tau \leq 90$ in the unforced case and for $\tau > 65$ in the weakly forced case. There is little evidence of self-similarity in the dissipation-rate evolution in the strongly forced case, although again $\mathcal{E}/(U_0^3\beta^2)$ is approximately constant for $40 < \tau < 60$. Note that the scaling with $U_0^3\beta^2$ has eliminated most of the variation in the magnitude of $\mathcal{E}$ among the different wakes. Compare the variation between the curves in figure 2(d) to the factor of 23 variation of β^2 among the three wakes.

The self-similarity of the unforced and weakly forced flows is further supported by the collapse of the mean velocity and Reynolds stress profiles when plotted in similarity coordinates. Shown in figure 3 are the mean velocity and streamwise velocity variance at four times, approximately equally spaced through the self-similar period, in both the unforced and weakly forced flows. The collapse of these curves in the unforced flow is good. In the weakly forced flow, there is more variation among the curves, especially for the mean velocity. This, however, may be a result of the inadequate statistical sample of the largest scales, which are larger in the forced cases. Profiles from times outside of the self-similar periods (not shown) do not collapse nearly as well. As in the mixing layer simulations in Rogers & Moser (1994), the breakdown of self-similarity at late times appears to occur because the finite size of the computational domain begins to affect the dynamics of the largest scales of motion in the flow. In the strongly forced flow, the mean and variance profiles also collapse fairly well during the brief approximately self-similar period ($40 \leq \tau \leq 58$).

It is evident from the favorable comparison of the predictions of the hypothesis and the data (especially the collapse of the mean velocity and Reynolds stresses) that the evolution of individual simulations are self-similar during a finite time domain. By examining all the measures of self-similarity presented in this section, especially the collapse of the mean velocity and Reynolds stress profiles discussed above, periods of self-similarity have been defined for each of the three simulated wake flows. For the unforced wake, the period of self-similarity has been determined to be $42.8 < \tau < 91.5$ and the value of β based on the wake growth rate during this period is 0.12. For the weakly forced wake, self-similarity is achieved during $64.5 < \tau < 120.9$ and $\beta = 0.21$. For the strongly forced case, a brief period of approximate self-similarity is found when $39.9 < \tau < 58.3$, during which $\beta = 0.58$. These time intervals are used to generate the time-averaged profiles presented later in this paper. The precisely quoted time limits given above correspond to the times of saved restart files from each simulation. In reality the approach and departure from self-similarity is fairly gradual and deciding which fields are within the self-similar period is somewhat subjective.

3.3. *Comparing different wakes*

Since the statistical quantities collapse in similarity coordinates, they can also be averaged in time over the self-similar period to reduce the statistical noise in the profiles. The profiles from the two sides of the wake are also averaged since they are all statis-

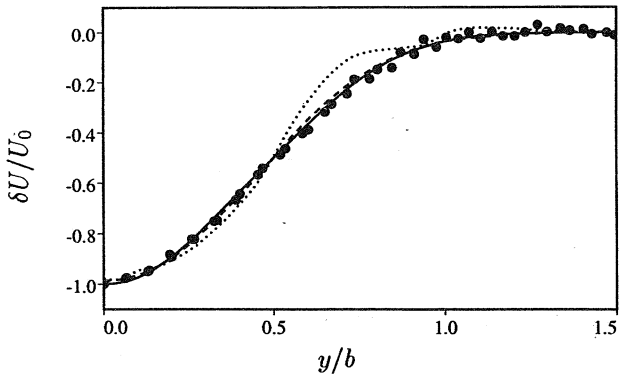

FIGURE 4. Comparison of time-averaged (in scaled coordinates) wake deficit profiles from the ——— unforced, – – – – weakly forced, and ····· strongly forced wake simulations, and • the experiments of Weygandt & Mehta (1993).

tically symmetric or antisymmetric about the centerline. The results of such averaging are shown in figures 4 and 5 for the mean velocity and Reynolds stress components, respectively. Also shown are the data from Weygandt & Mehta (1993). The Reynolds stress components have been scaled in the conventional way with U_0^2.

The agreement between the mean velocity profiles from the experimental and the unforced and weakly forced computations is very good. However, the mean profile from the strongly forced flow does not agree as well, nor is it as smooth. This is presumably because the simulations provide a poor statistical sample of the large structures that dominate the forced flow (see §4).

As can be seen in figure 5, the conventional scaling of the Reynolds stresses does not collapse the data from various wakes. Their is a marked increase in magnitude of all Reynolds stress components with increasing forcing level, with the experimental data generally falling between the unforced and weakly forced flows. The Reynolds stress levels in the strongly forced case are nearly an order of magnitude larger than those of the unforced case when scaled in this way. Clearly, this common scaling does not allow data from wakes with different growth rates to be effectively compared.

As indicated by the analysis in §3.1, it may be possible to collapse the different Reynolds stress profiles by including factors of the dimensionless growth rate β in the scaling. The simulation data can be used to determine the appropriate factors of β to include in the scaling to achieve the best overall collapse of the profiles. By using $U_0^2\beta$ and $U_0^2\beta^2$ to normalize the Reynolds stress profiles, it is possible to obtain approximate collapse of the different wake data, as shown in figure 6. Note that because the self-similarity is only approximate in the strongly forced case, less weight should be put on achieving collapse for this case when choosing the appropriate powers of β in the scalings. The selected scalings, which minimize the variation of the similarity profiles among the different wakes, have been listed in the fourth column of table 1.

The choice of the scaling for the Reynolds shear stress is also motivated by the observation that the mean velocity profiles collapse (figure 4), which implies that the shear stress profiles should collapse with the $U_0^2\beta$ scaling (see §3.1). Indeed, in figure 6d, the Reynolds shear stress profiles of the unforced and weakly forced wakes collapse with the experiments from Weygandt & Mehta (1993). The Reynolds stress profile for the strongly forced wake does not collapse as well with the others, which is consistent with the poorer collapse of the mean profile. Note that the scatter between the scaled Reynolds shear stress curves is greater than that among the scaled mean profiles. The viscous terms in

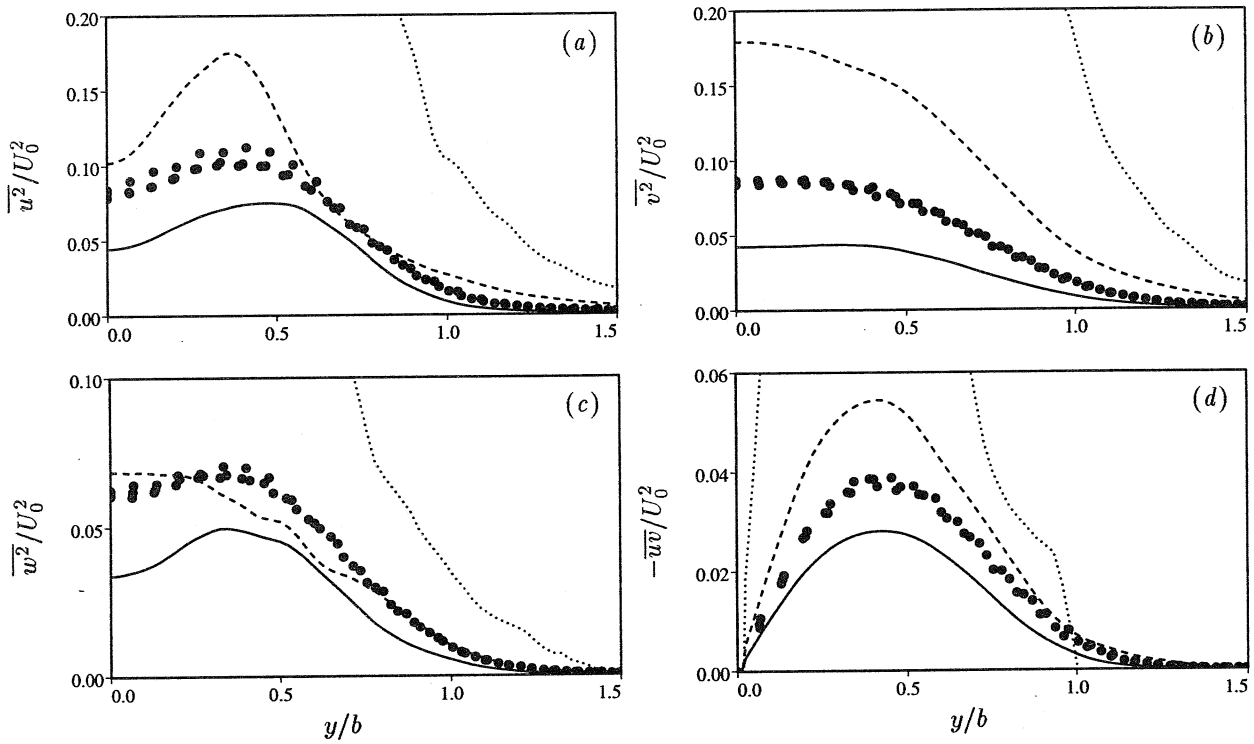

FIGURE 5. Comparison of the time-averaged (in scaled coordinates) components of the Reynolds stress tensor normalized by U_0^2 from the ——— unforced, ---- weakly forced, and ····· strongly forced wake simulations, and • the experiments of Weygandt & Mehta (1993).

the mean momentum equation are indeed small, and this slightly poorer collapse is a result of imperfect self-similarity. Collapse for the normal components of the Reynolds stress is not as good as for the shear stress. For the normal stress components, the scaled magnitudes are more or less consistent among the different wakes, but the profile shapes are not. This is to be expected given the growth rate dependence of the similarity equations (3.25) - (3.25). A similar variation in the shapes of the $\overline{u^2}$ profiles in different wakes was reported in Wygnanski *et al.* (1986).

In §3.1, specific scalings for each of the terms in the Reynolds stress transport equations were proposed based on the results of the three wake simulations discussed here. Shown in figure 7 are examples of the results of this scaling. Keeping in mind that the goal of the scaling is to eliminate the gross variations in magnitude among the three simulated wakes, it is apparent that the selected growth-rate scaling has succeeded for the $\overline{u^2}$ production and dissipation and the $\overline{v^2}$ pressure-strain (figures 7a, b, and c). This is not surprising for the production since it is just the product of the Reynolds shear stress and the mean velocity gradient, both of which are universal or near universal (see figures 4 and 6 and §3.1). The large peak in the strongly forced curve is due to the poorer collapse of $\overline{uv}$ and δU for the strongly forced case (see figure 6).

The time derivative of $\overline{uv}$ (figure 7d), however, is not as well scaled. There is a systematic increase in the magnitude of the curves with forcing level that could be eliminated by scaling with β^3 rather than β^2. But scaling $\overline{uv}$ with β (see table 1) implies the β^2 scaling for the time derivative. In fact, if the $\overline{uv}$ profile is universal as argued previously, then its time derivative should also be universal when scaled with β^2. The poor quality of

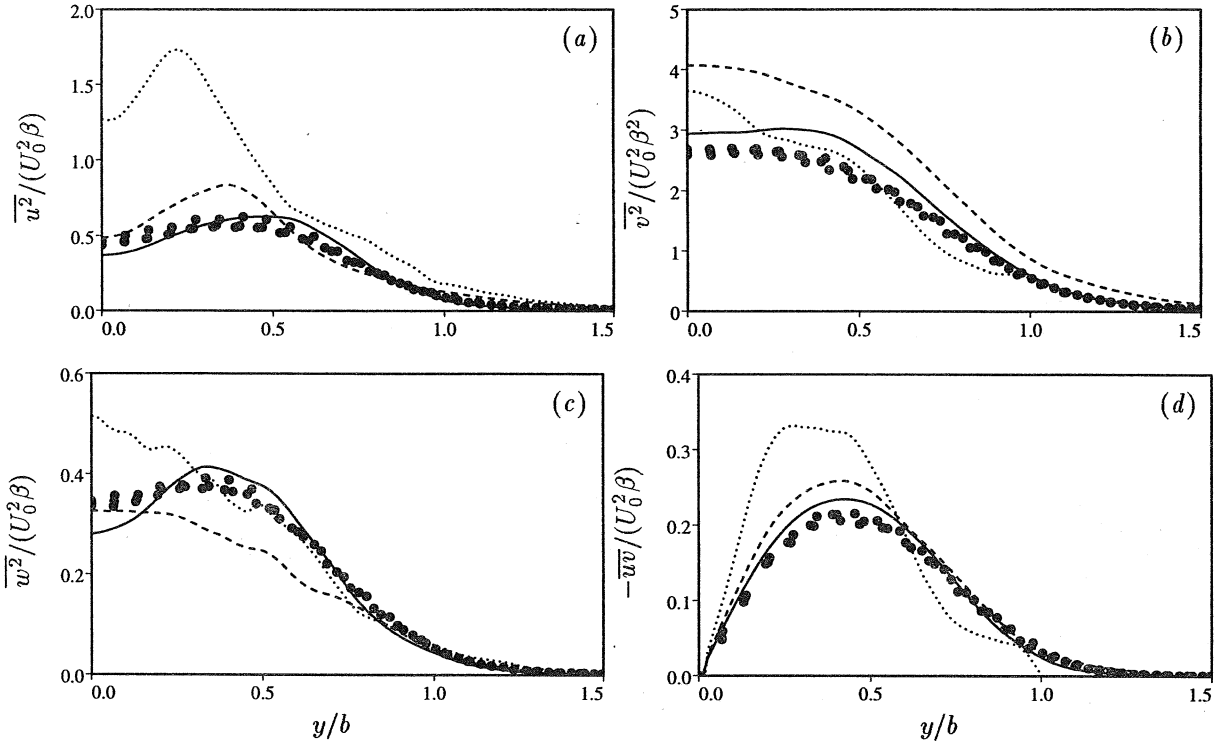

FIGURE 6. Comparison of the time-averaged (in scaled coordinates) profiles of $\overline{u^2}$, $\overline{v^2}$, $\overline{w^2}$, and $\overline{uv}$ normalized by $U_0^2\beta$ ($U_0^2\beta^2$ for $\overline{v^2}$) from the ——— unforced, - - - - weakly forced, and ····· strongly forced wake simulations, and • the experiments of Weygandt & Mehta (1993).

the scaling for the time derivative suggests a lack of statistical sample and/or imperfect self-similarity in one or more of the simulated wakes (perhaps this is also responsible for the imperfect collapse of the Reynolds shear stress profiles).

In figure 7e, the $\overline{uv}$ pressure diffusion magnitudes have been nicely scaled using $U_0^3\beta^3$, although a β^2 scaling would have been more pleasing as it would have removed a β factor from the profile equation (3.25). There is also a large qualitative difference between the pressure diffusion curves and it is not clear what this implies. Finally, examining the turbulent diffusion of $\overline{uv}$ profiles (figure 7f), the unforced and weakly forced profiles scale well, and are qualitatively similar. However, the profile from the strongly forced flow is qualitatively different and much larger in magnitude. Since self-similarity in the strongly forced wake is suspect, the scaling for the turbulent diffusion was selected to bring the unforced and weakly forced cases together, without regard to the strongly forced wake. Note that similar plots for the other terms in the Reynolds-stress balance have been used to obtain the rest of the scalings given in column 4 of table 1.

3.4. *The role of two-dimensional fluctuations*

As discussed in §2, the difference between the three simulated wakes discussed in this paper is that the "forced" simulations had amplified two-dimensional fluctuations in the initial conditions. Since this has produced such dramatic differences in the turbulence statistics and particularly the growth rate, the direct contribution of the two-dimensional fluctuations to the various statistics is of great interest. However, when considering

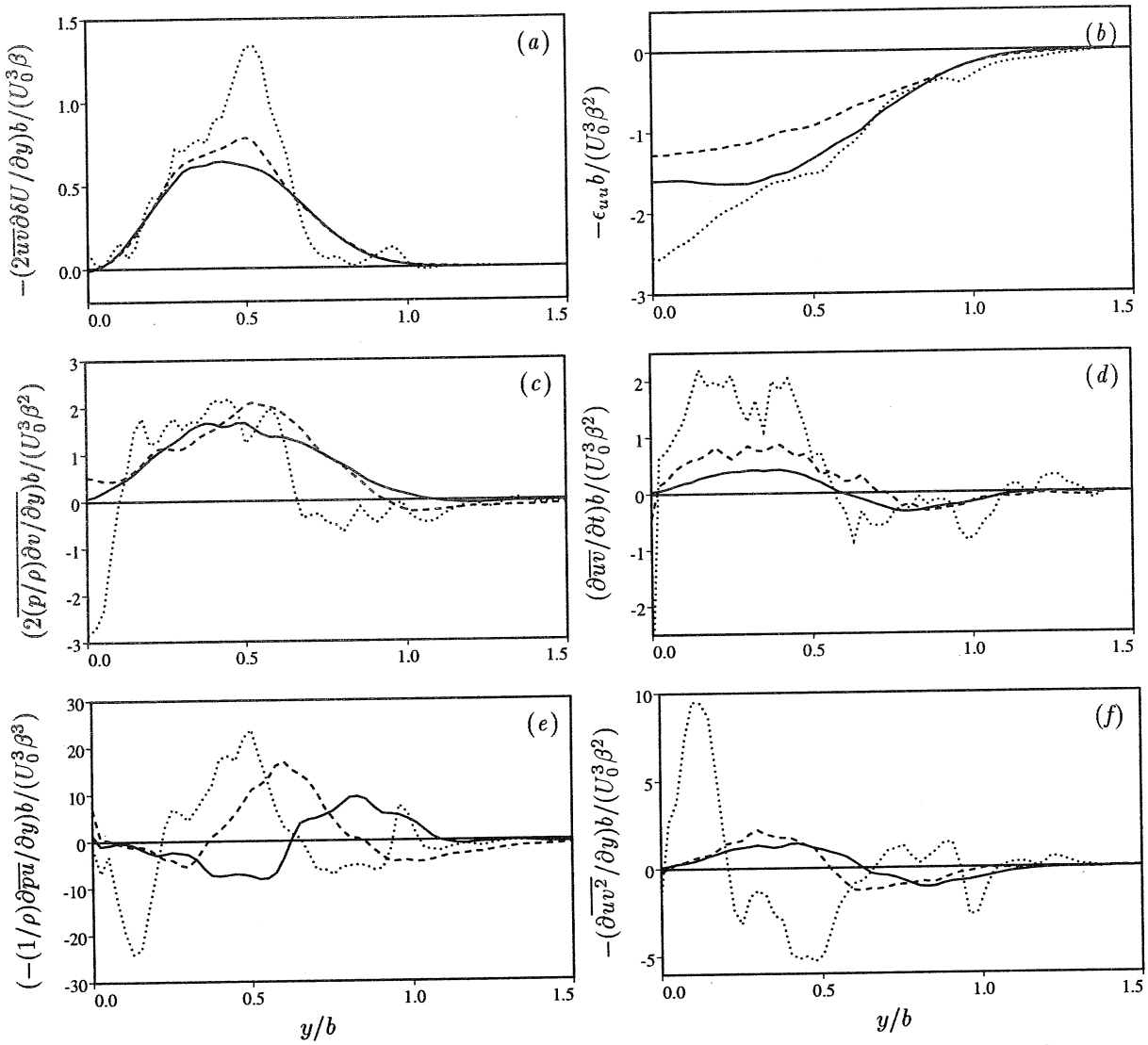

FIGURE 7. Comparison of various terms in the Reynolds stress balance equations from the ——— unforced, - - - - weakly forced, and ····· strongly forced wake simulations when scaled as in the fourth column of table 1. Shown are: (*a*) production of $\overline{u^2}$, (*b*) dissipation of $\overline{u^2}$, (*c*) $\overline{v^2}$ pressure-strain term, (*d*) time derivative of $\overline{uv}$, (*e*) pressure diffusion of $\overline{uv}$, and (*f*) turbulent diffusion of $\overline{uv}$.

the two-dimensional contribution to a self-similar plane wake a conceptual problem is encountered.

As pointed out in §3.2, the simulations can only model a self-similar time-developing wake of infinite streamwise and spanwise extent if the turbulence scales are significantly smaller than the domain size. It is this difference between the finite-domain computation and the infinite-domain flow that causes a problem in defining the contribution of two-dimensional perturbations. In the computations, the two-dimensional fluctuations are well defined as the average over the spanwise domain, which has length L_z. If L_z is allowed to go to infinity, this average (of the velocity say) will go to zero like $L_z^{-1/2}$

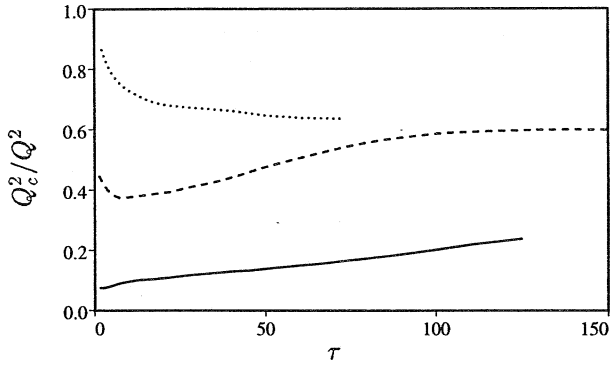

FIGURE 8. Evolution of the ratio of the cross-stream integrated spanwise coherent ($\alpha_f = 4$) contribution q_c^2 to the total cross-stream integrated q^2 in the ——— unforced, - - - - weakly forced, and ····· strongly forced wake simulations.

unless there are spanwise coherent fluctuations with infinite correlation length. In a truly turbulent flow such extreme spanwise coherence is not expected. Even the coherent structures common in free-shear flows become uncorrelated in the span at large enough separations, as suggested by the occurrence of dislocations in such structures as reported by Browand & Troutt (1980)). Thus, the contribution of the two-dimensional fluctuations to the energy density or any other quadratic quantity should go to zero like $1/L_z$. Such box-size-dependent measures of two-dimensionality are clearly not useful when investigating the relative importance of spanwise-coherent "two-dimensional" fluctuations. Indeed, if this subtlety had been fully recognized sooner, the "forced" initial conditions might have been designed differently.

To address this problem it is necessary to reconsider our intentions in studying "two-dimensional" fluctuations. In the current context, the interest is in fluctuations with a large spanwise spatial coherence. One way to define such fluctuations would be to apply a spanwise low-pass spatial filter with some filter width L_f; the resulting field would be approximately two dimensional provided L_f was large compared to the integral scale of the turbulence. The finite-domain spanwise average used in the simulations is an approximation of this, with L_z playing the role of L_f. However, the introduction of a filter width complicates the expected self-similar behavior of the statistics of the spanwise filtered field. Consider the filtered contribution q_f^2 to q^2 (twice the energy density), which must go like $1/L_f$. Thus, for a self-similar flow,

$$q_f^2 \propto \frac{U_0^2 b}{L_f}\,, \tag{3.28}$$

while the total q^2 evolves like U_0^2. Therefore the ratio q_f^2/q^2 will grow like b, the wake thickness, unless the filter width is also time dependent. Unfortunately, the computational domain width L_z cannot be time dependent. For the spanwise coherent contribution to be useful in the analysis to follow, such ratios should not evolve in time.

Another way to define the spanwise coherent fluctuations is as those fluctuations with a spanwise to streamwise aspect ratio (α) greater than some cutoff α_f. This is most easily accomplished by considering the Fourier representation of the velocity in the streamwise and spanwise directions (as is done in the numerical simulations), and defining the spanwise coherent fluctuations as those associated with fourier modes with $k_x > \alpha_f k_z$, where k_x and k_z are the streamwise and spanwise wavenumbers, respectively. Since this definition is based on an aspect ratio rather than a filter width, q_c^2/q^2 should be a con-

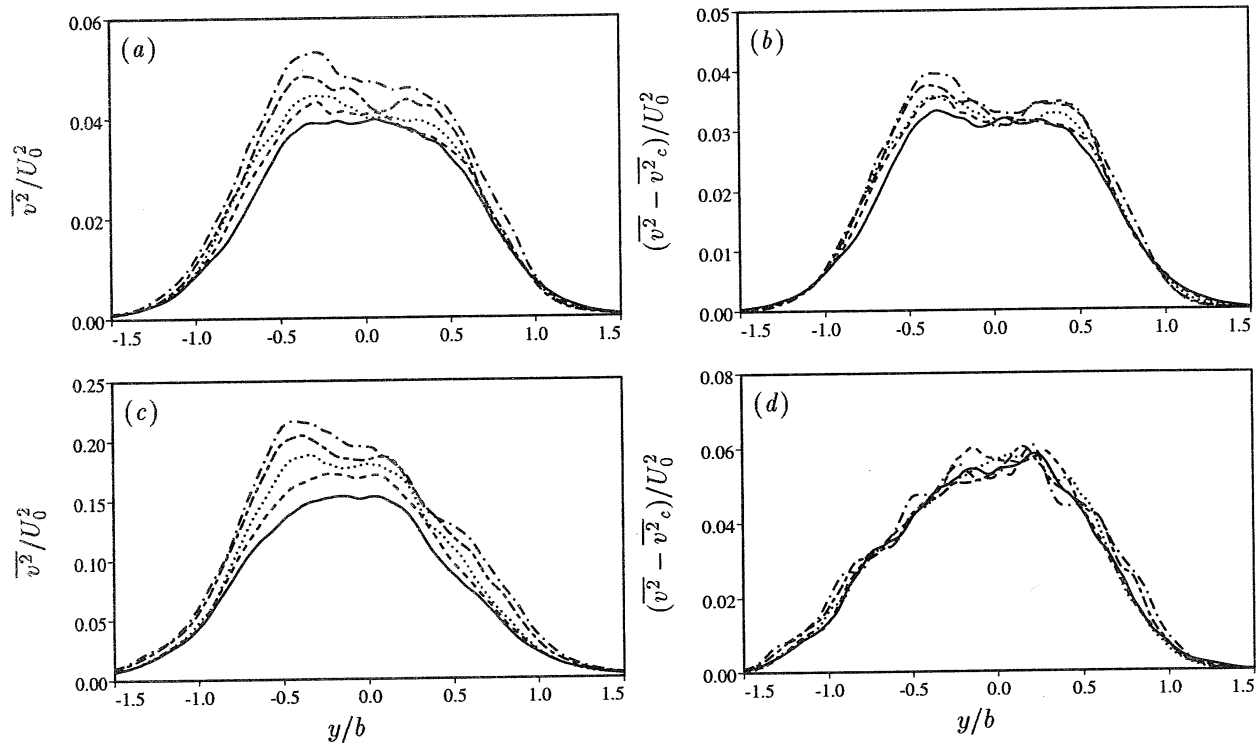

FIGURE 9. Collapse of (a,c) $\overline{v^2}/U_0^2$ and (b,d) $(\overline{v^2} - \overline{v^2}_c)/U_0^2$ in the (a,b) unforced and (c,d) weakly forced wakes. Profiles from the unforced and weakly forced wakes were taken at at ——— $\tau = 42.8$ and 64.5, - - - - $\tau = 51.0$ and 73.6, ····· $\tau = 62.4$ and 86.6, —— — $\tau = 74.9$ and 105.6,and —·— $\tau = 91.5$ and 120.9, respectively.

stant in a self-similar wake (the subscript c denotes the contribution of spanwise coherent fluctuations defined this way), and the same will be true for other quadratic quantities. Because of this desirable property, this aspect ratio definition will be used to study the contribution of spanwise coherent fluctuations. For the results presented below, $\alpha_f = 4$. Other values have also been tried (2 and 8) with no qualitative changes in the results.

The evolution of the ratio Q_c^2/Q^2, where Q_c^2 and Q^2 are integrals of the coherent and total (respectively) q^2 across the wake, is shown in figure 8 for the three simulations. It is interesting that the proportion of coherent energy continues to rise throughout the self-similar period in the unforced wake, suggesting that the unforced wake is not exactly self-similar after all. In contrast, in the weakly forced wake this ratio does become constant at around $\tau = 100$. For the strongly forced flow Q_c^2/Q^2 appears to be approaching approximately the same value as in the weakly forced flow. It is possible that the unforced flow would also ultimately reach the same value of this ratio, although this is far from certain. Thus, it might be possible that there is a universal value for the ratio of spanwise coherent energy to total energy (for a given α_f) in a truly self-similar wake. Note that this would not imply that other quantities must be universal, indeed the growth rates and many other quantities as well as the structure (see §4) of the weakly and strongly forced wakes differ.

In both the unforced and weakly forced flows, the Reynolds stress component with the worst self-similar collapse is $\overline{v^2}$ (see figure 9a and c). Throughout the self-similar period in both flows, there is a monotonic increase of the scaled $\overline{v^2}$ profile. However, when the $\overline{v^2}_c$ contribution is removed (figure 9b and d), the curves collapse very well. This is

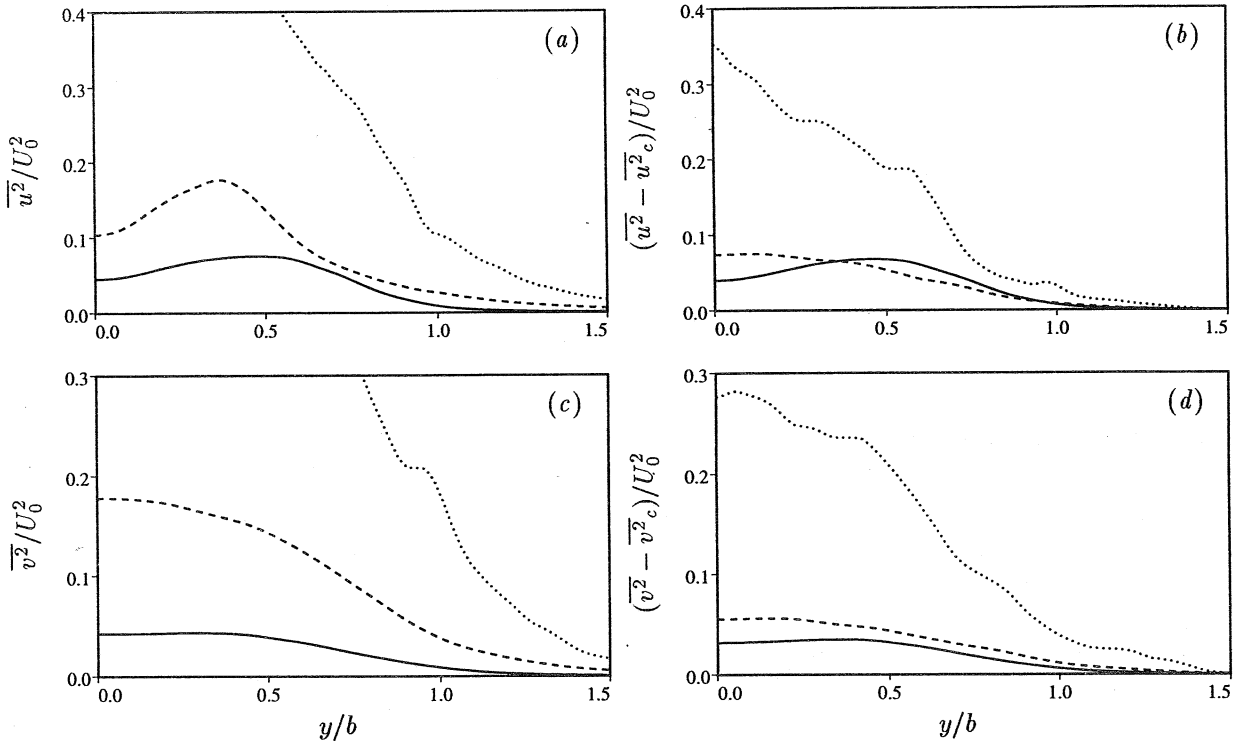

FIGURE 10. Comparison of (*a*) $\overline{u^2}$, (*b*) $\overline{u^2}-\overline{u^2}_c$, (*c*) $\overline{v^2}$ and (*d*) $\overline{v^2}-\overline{v^2}_c$ normalized by U_0^2 from the ——— unforced, - - - - weakly forced, and ····· strongly forced wake simulations.

consistent with the Q_c^2/Q^2 evolution for the unforced case. In the weakly forced flow, Q_c^2/Q^2 plateaus only toward the end of the self-similar period as shown in figure 8, and since $\overline{v^2}$ does not dominate q^2, it is possible for this lack of structural self-similarity to be more pronounced in $\overline{v^2}$ than in q^2. In any case, it is clear that the spanwise coherent fluctuations are not yet completely self-similar in these flows, and this may contribute to a variety of minor inconsistencies in the self-similarity as discussed in the previous sections.

It was noted in §3.3 that the Reynolds stress components had vastly different magnitudes among the three wakes, and that this could largely be scaled out using the growth rate β. These large differences are at least in part due to the contribution of the spanwise coherent fluctuations. Shown in figure 10 are the averaged $\overline{u^2}$ and $\overline{v^2}$ profiles (without the β scaling) along with the profiles with the $\overline{u^2}_c$ and $\overline{v^2}_c$ contributions removed. Removing the coherent contribution greatly decreases the variation among the different wakes. In fact, if the selection of the β scaling discussed in §3.1 were based on $\overline{v^2}-\overline{v^2}_c$ a factor of β rather than β^2 would have been chosen. For $\overline{u^2}-\overline{u^2}_c$ and $\overline{w^2}-\overline{w^2}_c$ the best collapse still results from the β scaling used in §3.1, but for $\overline{uv}-\overline{uv}_c$ there are no factors of β required to account for magnitude variation among the flows. The fact that the spanwise incoherent fluctuations (which are expected to dominate the dissipation) yield lower powers of β in the scalings than the total $\overline{v^2}$ and $\overline{uv}$ is probably responsible for the "inconvenient" scaling of the ϵ_{vv} and ϵ_{uv} terms that result in the $1/\beta$ coefficient appearing on d_v and d_{uv} in (3.25) and (3.25).

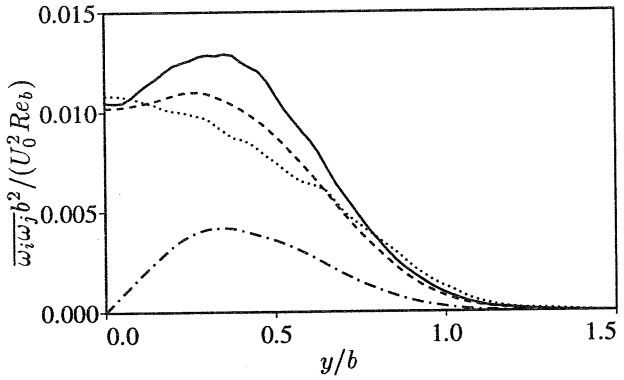

FIGURE 11. Time-averaged (in scaled coordinates) vorticity correlation tensor profiles $\overline{\omega_i\omega_j}$ for the unforced wake. ——— $\overline{\omega_x^2}$, - - - - $\overline{\omega_y^2}$, ····· $\overline{\omega_z^2}$, —·— $\overline{\omega_x\omega_y}$.

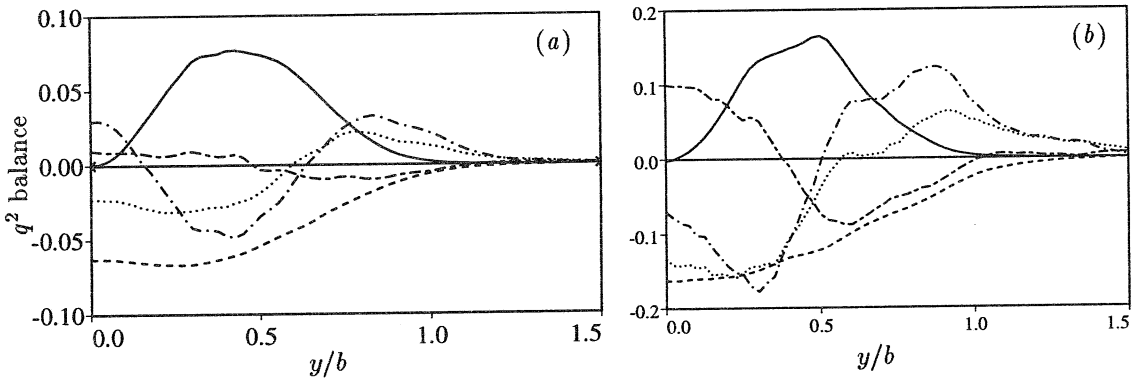

FIGURE 12. Terms in the $\overline{q^2}$ balance equation, scaled by U_0^3/b for (a) the unforced wake and (b) the weakly forced wake, ——— production - - - - dissipation ····· time derivative, —·— turbulent diffusion, and — - — pressure diffusion.

3.5. *Other statistics*

In addition to velocity and Reynolds stress statistics, vorticity statistics can be obtained from the simulations. As in Rogers & Moser (1994), the scaling of $\mathcal{E}$ with U_0^3 implies that the vorticity variances should scale like $Re_b U_0^2/b^2$, where $Re_b = U_0 b/\nu$. However, since Re_b is a constant in the self-similar wakes studied here, the Reynolds number factor would only be important when comparing wakes at different Reynolds numbers. As an example, the vorticity variances averaged over the self-similar period in the unforced flow are shown in figure 11. The relative magnitudes of the variances of the vorticity components are in general agreement with those found in previous computations of homogeneous shear flows (Rogers & Moin 1987) and plane mixing layers (Rogers & Moser 1994).

The time averages of the terms in the balance equation for q^2 over the self-similar periods of the unforced and weakly forced wakes are shown in figure 12. (Note that the balances for the individual normal Reynolds stress components and the Reynolds shear stress are given in Appendix A, along with the definitions of the balance terms. The balance for the strongly forced case is not included because the self-similarity in this case is only approximate and of short duration). Since the shear is zero at the center of the wake, the production is zero there. Production of $\overline{q^2}$ thus peaks in the maximum shear region and is transported away by turbulent diffusion. Pressure diffusion provides transport to the center of the wake, although in the unforced case this transport is

rather small and the turbulent diffusion is primarily responsible for transport to the wake centerline. The transport of $\overline{q^2}$ by turbulent diffusion to the edge of the wake is responsible for nearly all of the growth in the width of the $\overline{q^2}$ profile. The transport of energy away from the centerline by the turbulent diffusion in the weakly forced case may be related to the large amount of turbulent kinetic energy added there initially by the forcing. The negative time derivative near the center of the wake produces the t^{-1} decay in the maximum $\overline{q^2}$, and the growth in the width of the turbulent region is reflected in the positive time derivative at the edge of the wake. The overall level of the curves in figure 12(b) is larger than that in figure 12(a) because the increase associated with the larger growth rate β has not been scaled out as it was in in figure 7 (note table 1 indicates different powers of β are required to compare different terms in the balance).

For a self-similar wake the time derivative can be computed directly from the $\overline{q^2} = U_0^2 h(\eta)$ profile ($\eta = y/b$), with the result

$$\frac{b}{U_0^3}\frac{\partial \overline{q^2}}{\partial t} = -\beta(2h + \eta h') \,. \tag{3.29}$$

Using the unforced case as an example, at the centerline $h = \overline{q^2}/U_0^2$ is 0.12 and $\beta = 0.12$, resulting in a centerline value of the time derivative of 0.029. This is somewhat larger than the value (0.023) computed from the simulation data and plotted in figure 12. The discrepancy is a measure of the departure of the simulation from self-similarity, and the adequacy of the statistical sample.

4. Structures

The large statistical differences between the three wakes discussed in §3 are a manifestation of the differences in the structure of the turbulence in these flows. This difference can be seen in figure 13, where spanwise vorticity contours in x–y planes of all three flows are shown. In the strongly forced case, there are concentrations of vorticity fluctuations that occur alternately on one side of the wake or the other, similar to the Karman street commonly observed in transitional wakes. By examining other x–y planes (not shown), one can determine that these large-scale features are spanwise coherent. The vorticity concentrations are also accompanied by large incursions of irrotational fluid into the wake. In contrast, the unforced wake exhibits no such vorticity concentrations, and relatively small incursions of irrotational fluid. It appears to consist of a slab of turbulence with undulating boundaries. The weakly forced flow is intermediate between the other two cases. Forcing was also found to produce large-scale structures similar to those in transitional flows in the turbulent mixing layers of Rogers & Moser (1994).

Another striking difference between the two flows is that the forced flows appear to have vorticity fluctuations of smaller scale, especially the strongly forced flow. This is consistent with the appearance of the streamwise spatial spectra in figure 1 and the fact that finer spatial resolution was required to compute the forced flow accurately. Comparing figure 13(a) and figure 13(c), it appears that the strongly forced flow has a larger turbulence Reynolds number than the unforced flow since the ratio of the size of the large-scale features to the size of the small-scale features is greater. Indeed the centerline value of the turbulence Reynolds number $q^4/(\epsilon\nu)$ is an order of magnitude larger in the strongly forced case than in the unforced case ($q^4/(\epsilon\nu) = 4000$, 1500, and 460 for strongly forced, weakly forced, and unforced wakes, respectively) despite the fact that the Reynolds numbers based on $\dot{m}$ are the same in all three flows.

The mixing layer simulations of Rogers & Moser (1994, Rogers & Moser (1993) suggest

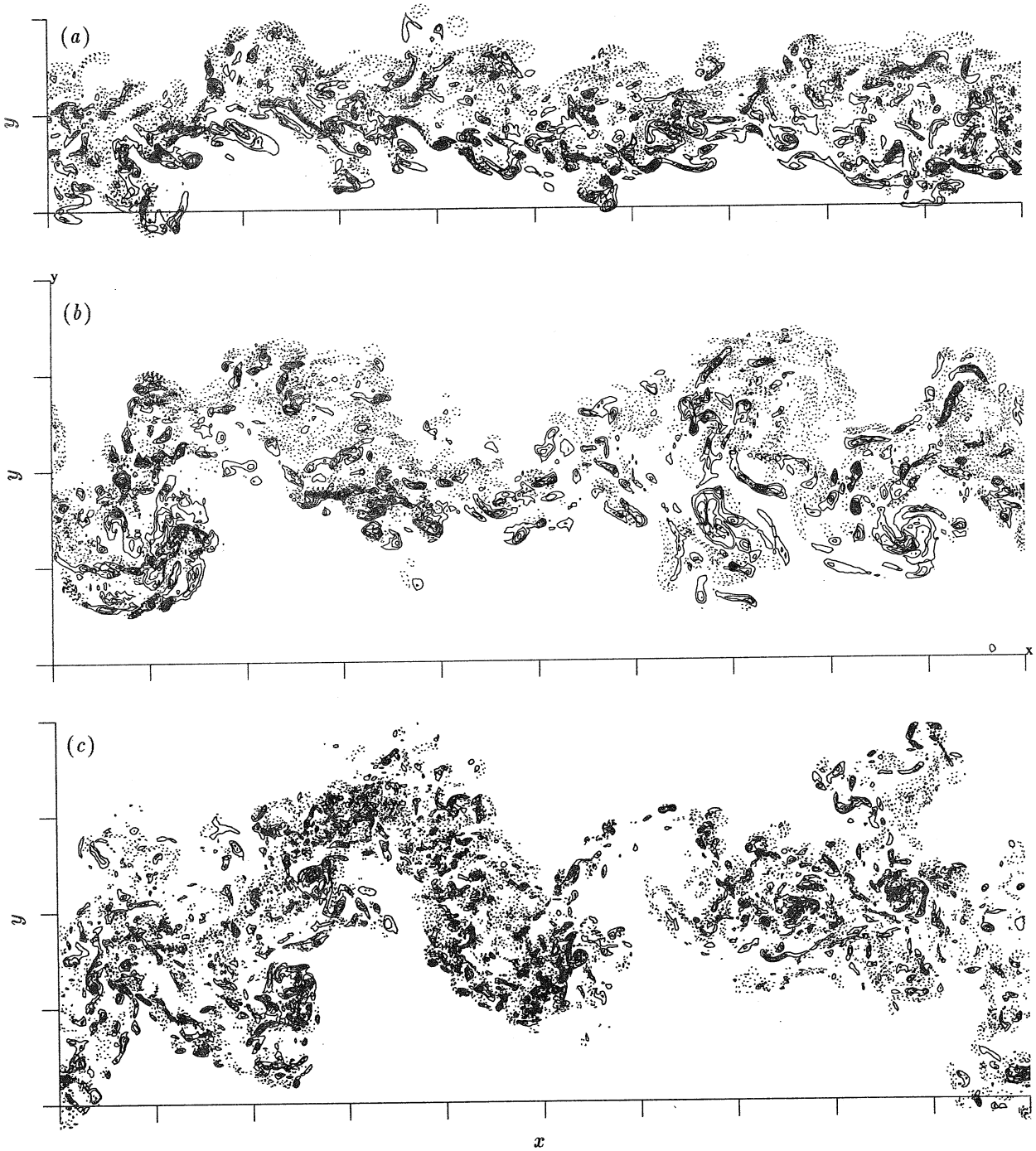

FIGURE 13. Contours of spanwise vorticity in an x–y plane in (a) the unforced flow at $\tau = 91.5$, (b) the weakly forced flow at $\tau = 116$, and (c) the strongly forced flow at $\tau = 50.0$. The contour increments are (a) $2.5U_0/b$, (b) $5U_0/b$ and (c) $20U_0/b$, and negative contours are dotted. Tic marks are at $5\dot{m}/U_d$ intervals.

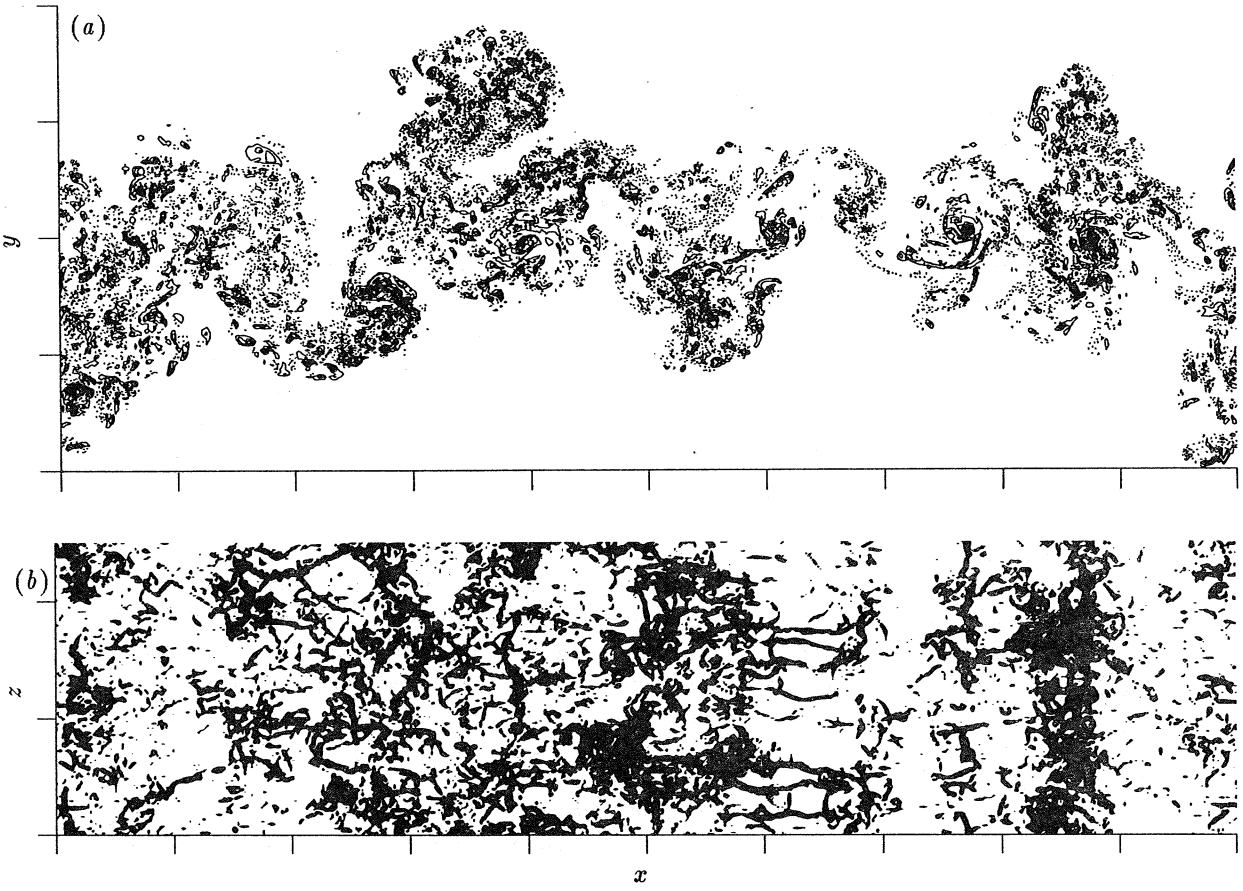

FIGURE 14. (*a*) Contours of spanwise vorticity in an x–y plane (contour increment of $10U_0/b$) and (*b*) top view of regions where enstrophy ($\omega_i\omega_i$) is larger than $8700U_0^2/b^2$ in the strongly forced flow at $\tau = 26.3$. Tic marks are at $5U_d/\dot{m}$ intervals.

that whenever there is a flow region that is dominated by large-scale strain, but largely devoid of (spanwise) vorticity, it is likely that long coherent vortices aligned with the extensional strain (so-called rib vortices), will develop. Such a region might be expected between the vortices in a Karman Street, and indeed rib vortices have been observed in simulations of transitional wakes (Lasheras & Meiburg 1990). A strain-dominated region of this type appears to exist in the forced flow shown in figure 13(*c*)(at $x \approx 30\dot{m}/U_d$), but no rib vortices were found at this time. However, at an earlier time ($\tau = 26.3$, figure 14), the strain-dominated region is also present and rib vortices occur there. The rib vortices can be seen in figure 14(*b*) as the long thin streamwise-oriented regions of large enstrophy at $x \approx 32\dot{m}/U_d$. These vortices span the strain-dominated region, and do not occur elsewhere in the strongly forced flow or anywhere in the weakly forced or unforced flow, which have no such strain-dominated regions. The reason for the disappearance of the rib vortices at later times has not yet been investigated.

5. Conclusions

The evolution of self-similar turbulent plane wakes has been studied using three direct numerical simulations of time-developing wakes. Each simulation was initialized

using fields from a previously computed fully developed turbulent boundary layer, thus the simulations are time-developing models for the wake of a flat plate. In addition to the boundary layer turbulence, the energy in the two-dimensional disturbances was augmented in two of the simulations, with the strength of the augmentation differing in the two cases. This was done to mimic the experimental situation in which nearly two-dimensional disturbances can be introduced into the flow as a result of the receptivity of the splitter-plate tip to acoustic disturbances in the facility.

Of the three simulated wakes, the unforced and weakly forced flows exhibit an extended period of self-similarity before the finite computational domain size constrains the flow evolution. In addition, the strongly forced flow has a short period of approximate self-similarity, and the results of recent large eddy simulations suggest that this self-similar period would endure longer in a larger computational domain (Ghosal & Rogers 1996). While all three flows are at least approximately self-similar, they have markedly different growth rates, turbulence Reynolds numbers, Reynolds stress tensors, and large-scale structures. Thus, consistent with the analytical analysis of the governing equations and experimental observations in several spatially evolving plane wakes, it appears that multiple self-similar states are possible in this flow (if the normalized growth rates differ).

It is also evident from the analysis of the governing equations for the mean flow and Reynolds stress tensor that the scaling for many of the terms in the equations is ambiguous. This is due to the existence of two velocity scales (the growth rate and the deficit velocity), or equivalently, the existence of an extra parameter (the nondimensional growth rate parameter β). It was shown that sensible scalings could be found to minimize the differences in the scaled quantities from the different wake flows. The resulting scalings amount to including various factors of β in the conventional scalings based on the velocity deficit.

However, when writing the scaled self-similar Reynolds stress equations using these scalings, factors of β appear in the equations. Further, there is no choice of scalings for which factors of β are absent. Thus, while plane wakes with different growth rates can be individually *self*-similar, they can not be dynamically similar to each other. This implies that there is at least a one-parameter family of possible high-Reynolds number self-similar plane wakes, parameterized by the growth rate (β). Further, the analysis does not *require* that wakes with the same growth rate are similar; it says only that this is allowed. Despite the lack of dynamic-similarity, it does appear from both experiments and the current simulations that the mean velocity profile in self-similar plane wakes is universal.

One measure of the structural similarity of the three wakes is the ratio of the energy in the "spanwise coherent" fluctuations (defined in §3.4) to the total fluctuation energy. This ratio should be constant in a self-similar flow, and it is in the weakly forced wake. In the strongly forced wake the ratio is evolving, but appears to be approaching the same value. In the unforced flow, the ratio is smaller but it continues to grow very slowly through the self-similar period. Thus, in this regard the unforced flow is going through a very slow transient as discussed above, although there is no evidence that this is changing the growth rate. This slow increase in the spanwise coherent energy fraction results in a slight monotonic increase in the scaled cross-stream fluctuation intensity $\overline{v^2}$, which has also been observed in experiments (Weygandt & Mehta 1993). It may be that in truly self-similar wakes, the spanwise coherent energy ratio is universal or nearly universal. The importance of the coherent fluctuations to the self-similar evolution of the wakes is emphasized by the fact that there is much less variation among the different wakes if only the incoherent fluctuations are included in the statistics.

The forcing also has an impact on the vortical structures in the flow, with the forced

flow exhibiting large-scale Karman-vortex-street-like structures similar to those observed in transitional wakes. No such organized structures were present in the unforced flow, where the vorticity was concentrated in a more or less uniform undulating slab without free-stream fluid penetrating deep into the layer. The organized large-scale structure of the strongly forced flow results in strain-dominated "braid" regions between large-scale structures. Early in the flow evolution it is possible to find streamwise "rib" vortices within the braid regions, although they do not appear to be as persistent as similar structures in forced mixing layers.

The forcing used in these computations has clearly resulted in qualitative differences in the turbulence. It impacts both the statistics and flow structure and these differences can be maintained for significant time periods, possibly indefinitely. The implications of these observations to the modeling of turbulent wakes are profound. In geometrically equivalent flow situations, it is apparently possible to get wakes with greatly differing growth rates and statistical and structural properties depending on uncontrolled and possibly unknown properties of the initial or inlet conditions. Worse, given the nature of the differences in the initial conditions in the flows studied here, it is likely that standard turbulence models (e.g. k–ϵ or Reynolds stress transport models), which are insensitive to the features of the initial or inlet conditions that control the state of the wake, would be incapable of predicting this flow.

We thank Professor W. K. George for his help in developing the self-similar analysis presented above for the temporally evolving plane wake and for his insightful comments regarding the evolution of the simulated wake flows. Much of the computations were performed on the NAS supercomputers at the NASA Ames Research Center.

Appendix A. Reynolds stress balances

The governing equation for the evolution of the Reynolds stresses in a time-developing plane wake can be written as

$$\frac{\partial \overline{u_i u_j}}{\partial t} = -\left(\overline{u_i u_l}\frac{\partial \overline{U_j}}{\partial x_l} + \overline{u_j u_l}\frac{\partial \overline{U_i}}{\partial x_l}\right) - \frac{\partial \overline{u_i u_j u_2}}{\partial x_2} - \left(\overline{u_j \frac{\partial (p/\rho)}{\partial x_i}} + \overline{u_i \frac{\partial (p/\rho)}{\partial x_j}}\right) + \nu \frac{\partial^2 \overline{u_i u_j}}{\partial^2 x_2} - 2\nu \overline{\frac{\partial u_i}{\partial x_l}\frac{\partial u_j}{\partial x_l}}. \quad \text{(A 1)}$$

The "time derivative" on the left is thus composed of "production", "turbulent diffusion", "velocity-pressure gradient", "viscous diffusion", and "dissipation" terms, where these terms are given in this order in the above equation (and include minus signs where present). It is also possible to further split the velocity-pressure gradient term into "pressure-strain" and "pressure diffusion" terms,

$$-\left(\overline{u_j \frac{\partial (p/\rho)}{\partial x_i}} + \overline{u_i \frac{\partial (p/\rho)}{\partial x_j}}\right) = \overline{\frac{p}{\rho}\left(\frac{\partial u_i}{\partial x_j} + \frac{\partial u_j}{\partial x_i}\right)} - \frac{1}{\rho}\left(\delta_{i2}\frac{\partial \overline{pu_j}}{\partial x_2} + \delta_{j2}\frac{\partial \overline{pu_i}}{\partial x_2}\right). \quad \text{(A 2)}$$

In these equations, only the mean velocity component U_1 is nonzero and due to homogeneity, derivatives of averaged quantities with respect to x_1 and x_3 are zero. Thus, there is no production term in the $\overline{u_2^2}$ and $\overline{u_3^2}$ equations and no pressure diffusion term in the $\overline{u_1^2}$ and $\overline{u_3^2}$ equations. The equation for $q^2 = \overline{u_i u_i}$ can be obtained by contracting the indices in the above equations. For this equation, the pressure-strain is zero and the velocity-pressure gradient term includes only pressure diffusion.

The profiles of each of the balance terms (scaled by U_0^3/b with no factors of β) in all

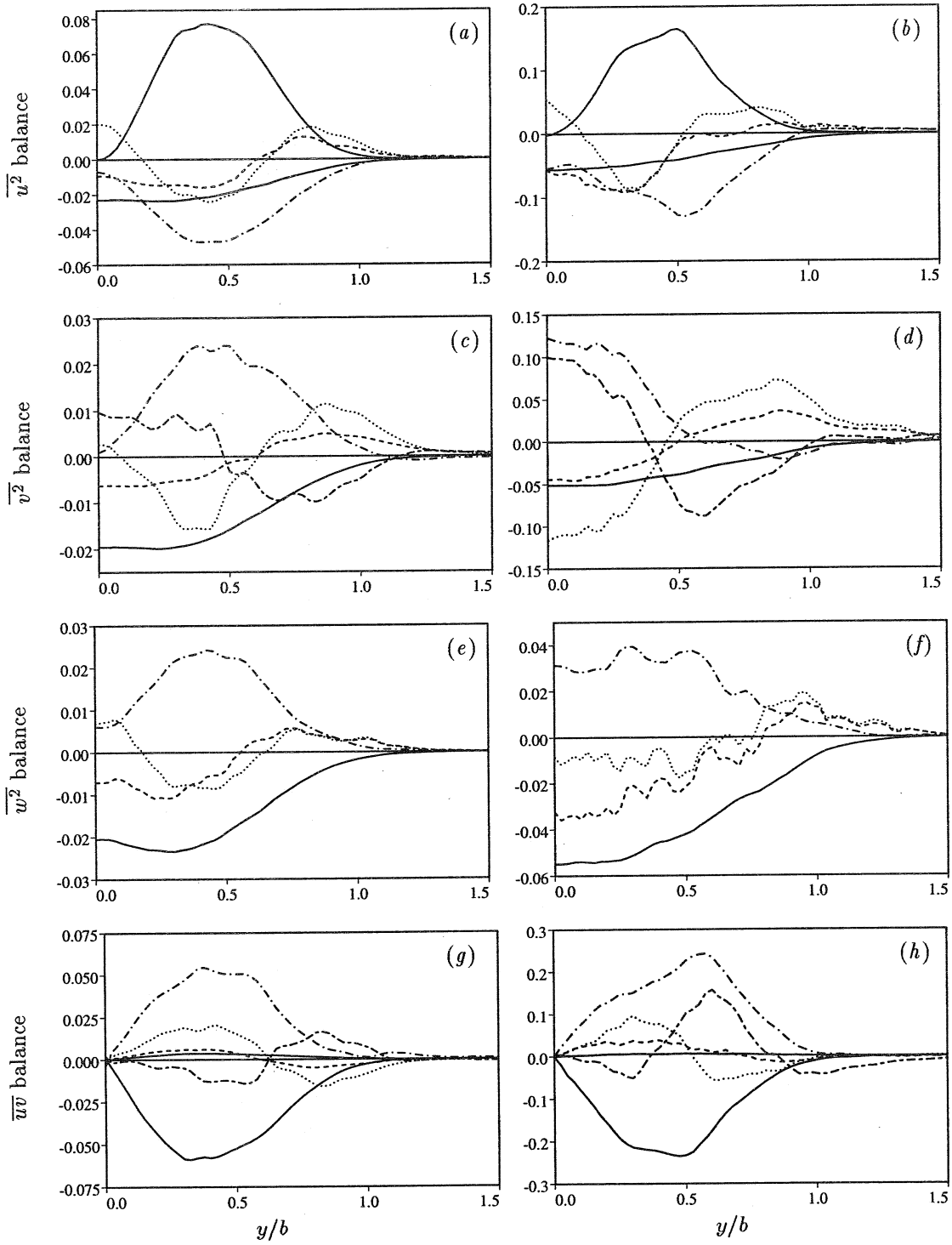

FIGURE 15. Reynolds stress balances for the (*a*),(*b*) $\overline{u^2}$, (*c*),(*d*) $\overline{v^2}$, (*e*),(*f*) $\overline{w^2}$, and (*g*),(*h*) $\overline{uv}$ equations for the unforced ((*a*), (*c*), (*e*), and (*g*)) and weakly forced ((*b*), (*d*), (*f*), and (*h*)) wakes. —— either production (positive curves in (*a*) and (*b*), negative in (*g*) and (*h*)) or dissipation (positive in (*g*) and (*h*), negative in all others), – – – – time derivative, ····· turbulent diffusion, —·— velocity-pressure gradient, and — – — pressure diffusion.

the Reynolds stress equations time averaged over the self-similar period (note that the q^2 balances were shown in figure 12) for the unforced and weakly forced wake simulations are shown in figure 15.† The viscous diffusion terms are not plotted because they are an order of magnitude smaller than any other term across the entire layer and thus cannot be distinguished from zero in the figure.‡

If the wakes considered here were exactly self-similar, then the centerline level of $\overline{u_i u_j}/U_0^2$ would remain unchanged. However, since U_0 decays in time, this does not imply that the scaled time derivative (dashed) curves in figure 15 should be zero at $\eta = y/b = 0$. It is possible to use the $\overline{u_i u_j}$ profiles shown in figure 5 with the assumption of self-similarity to derive the entire $\partial\overline{u_i u_j}/\partial t$ profiles, which can then be compared to those in figure 15 to obtain a measure of the departure of the simulations from self-similarity. Generalizing equation (3.29) by defining the functions f_{ij} and g_{ij},

$$f_{ij}(\eta) = \frac{\overline{u_i u_j}(\eta)}{U_0^2} \qquad g_{ij}(\eta) = \frac{b}{U_0^3}\frac{\partial\overline{u_i u_j}(\eta)}{\partial t}\,, \tag{A 3}$$

one obtains

$$g_{ij} = -\beta(2f_{ij} + \eta f'_{ij})\,. \tag{A 4}$$

At the centerline $g_{ij}(0) = -2\beta f_{ij}(0)$. Obtaining $f_{ij}(0)$ from figure 5 and β from §3.2 the computed values of $g_{ij}(0)$ can be seen to be in fairly good agreement with the values plotted in figure 15.

Appendix B. Similarity for a passive scalar field

A similarity analysis of the type presented in §3.1 can also be applied to the equations governing the evolution of a passive scalar quantity in the temporally evolving wake flow. In this appendix two different geometries for the passive scalar field are examined. First, the similarity analysis is applied to a two-stream passive scalar field in which the mean value of the passive scalar differs on the two sides of the wake. Physically, this corresponds to the wake behind a splitter plate separating two equal velocity streams, which each have a different level of the scalar. Next the similarity analysis is extended to a second geometry in which the mean value of the passive scalar on both sides of the wake is equal, but a surplus or deficit of the scalar occurs in the wake. Physically this geometry corresponds to a wake produced behind a hot/cold plane body or the wake produced by a plane body injecting a scalar into the field.

The equation governing the evolution of the mean value of the passive scalar in the temporally evolving wake is given by

$$\frac{\partial\Theta}{\partial t} = -\frac{\partial\overline{v\theta}}{\partial y} + \alpha\frac{\partial^2\Theta}{\partial y^2} \tag{B 1}$$

where Θ is the mean value of the passive scalar, θ is the scalar fluctuation, and α is the molecular diffusivity of the passive scalar. As in §3.1, it is hypothesized that the equation governing the mean scalar field in the two-stream geometry has a similarity solution of

† Those for the strongly forced wake flow show significant differences, including overall higher levels (no factors of β in the scaling) and turbulent and pressure diffusion dominating production and dissipation. They are not presented here because of the poorer self-similarity of the strongly forced flow.

‡ Note that this is not the case early in the flow evolution, when the initial boundary layer turbulence has significant viscous diffusion near the "wall", which has just been "removed".

the form

$$\Theta - \Theta_1 = Sc(t)sc(\eta_\theta) \tag{B 2a}$$

$$\overline{v\theta} = R_{v\theta}(t)r_{v\theta}(\eta_\theta)\,, \tag{B 2b}$$

where η_θ is a similarity coordinate based on a characteristic length scale for the passive scalar given by

$$\eta_\theta = \frac{y}{\delta_\theta} \tag{B 3}$$

and Θ_1 is the mean value of the passive scalar in the flow as $y \to -\infty$.

The hypothesized similarity solution given in equation (B 2) must satisfy the boundary conditions as $y \to \pm\infty$. Consequently, the scale for the mean value of the scalar variable must be proportional to the difference of the mean value of the scalar at the two limits; *i.e.*

$$Sc(t) \propto U_d\Theta = \Theta_2 - \Theta_1\,, \tag{B 4}$$

where Θ_2 is the mean value of the scalar as $y \to \infty$. It is conventional to define this condition as an equality so $sc(\eta_\theta)$ is a function which varies between 0 and 1.

Substituting the hypothesized similarity solutions into equation (B 1) one obtains

$$-\left[\frac{Sc}{\delta_\theta}\frac{d\delta_\theta}{dt}\right]\eta_\theta\frac{dsc}{d\eta_\theta} = -\left[\frac{R_{v\theta}}{\delta_\theta}\right]\frac{dr_{v\theta}}{d\eta_\theta} + \alpha\left[\frac{Sc}{\delta_\theta^2}\right]\frac{d^2sc}{d\eta_\theta^2} \tag{B 5}$$

The molecular diffusion terms in this equation are often neglected relative to the turbulent diffusion, but this is not necessary for a similarity solution to exist for this turbulent flow. Consequently, the diffusion terms are not neglected in this analysis.

The hypothesized similarity solutions are consistent with equation (B 1) if

$$\left[\frac{Sc}{\delta_\theta}\frac{d\delta_\theta}{dt}\right] \propto \left[\frac{R_{v\theta}}{\delta_\theta}\right] \propto \left[\frac{Sc}{\delta_\theta^2}\right]\,, \tag{B 6}$$

so that

$$R_{v\theta} \propto Sc\frac{d\delta_\theta}{dt} \propto U_d\Theta\frac{d\delta_\theta}{dt} \tag{B 7}$$

and

$$\frac{d\delta_\theta^2}{dt} = \text{constant}\,, \tag{B 8}$$

Therefore, the proposed similarity solutions are consistent with the equation if the growth rate of the length scale characteristic of the scalar field is given by

$$\delta_\theta \propto (t - t_{o\theta})^{1/2}\,, \tag{B 9}$$

analogous to the length scale for the velocity field. Note, equation (B 9) does not assume that the virtual origin of the scalar field coincides with the virtual origin of the velocity field. The relationship between the locations of these two virtual origins is deduced below by examining the evolution equation for the passive scalar flux.

As in §3.1, the analysis is next extended to the second-moment equations, here given by evolution equations for the scalar variance and turbulent scalar flux

$$\frac{\partial\overline{\theta^2}}{\partial t} = -2\overline{v\theta}\frac{\partial\Theta}{\partial y} - \frac{\partial\overline{v\theta^2}}{\partial y} + \alpha\frac{\partial^2\overline{\theta^2}}{\partial y^2} - \epsilon_\theta\,, \tag{B 10a}$$

$$\frac{\partial\overline{u\theta}}{\partial t} = -\frac{\overline{\theta}}{\rho}\frac{\overline{\partial p}}{\partial x} - \overline{v\theta}\frac{\partial\delta U}{\partial y} - \overline{uv}\frac{\partial\Theta}{\partial y} - \frac{\partial\overline{uv\theta}}{\partial y} + \alpha\frac{\partial}{\partial y}\overline{u\frac{\partial\theta}{\partial y}} + \nu\frac{\partial}{\partial y}\overline{\theta\frac{\partial u}{\partial y}} - \epsilon_{u\theta}\,, \tag{B 10b}$$

$$\frac{\partial \overline{v\theta}}{\partial t} = -\overline{\frac{\theta}{\rho}\frac{\partial p}{\partial y}} - \overline{v^2}\frac{\partial \Theta}{\partial y} - \frac{\partial \overline{v^2\theta}}{\partial y} + \alpha\frac{\partial}{\partial y}\overline{v\frac{\partial \theta}{\partial y}} + \nu\frac{\partial}{\partial y}\overline{\theta\frac{\partial v}{\partial y}} - \epsilon_{v\theta}\,, \tag{B 10c}$$

where ϵ_θ, $\epsilon_{u\theta}$, and $\epsilon_{v\theta}$ are dissipation rates given by

$$\epsilon_\theta = 2\alpha\left\{\overline{\left(\frac{\partial\theta}{\partial x}\right)^2} + \overline{\left(\frac{\partial\theta}{\partial y}\right)^2} + \overline{\left(\frac{\partial\theta}{\partial z}\right)^2}\right\}, \tag{B 11a}$$

$$\epsilon_{u\theta} = (\nu+\alpha)\left\{\overline{\frac{\partial u}{\partial x}\frac{\partial\theta}{\partial x}} + \overline{\frac{\partial u}{\partial y}\frac{\partial\theta}{\partial y}} + \overline{\frac{\partial u}{\partial z}\frac{\partial\theta}{\partial z}}\right\}, \tag{B 11b}$$

and

$$\epsilon_{v\theta} = (\nu+\alpha)\left\{\overline{\frac{\partial v}{\partial x}\frac{\partial\theta}{\partial x}} + \overline{\frac{\partial v}{\partial y}\frac{\partial\theta}{\partial y}} + \overline{\frac{\partial v}{\partial z}\frac{\partial\theta}{\partial z}}\right\}. \tag{B 11c}$$

Using the definitions given in table 1 in §3.1 and table 2 below, a similarity solution is possible when

$$\left[\frac{dV_\theta}{dt}\right] \propto \left[\frac{V_\theta}{\delta_\theta}\frac{d\delta_\theta}{dt}\right] \propto \left[\frac{Tt_\theta}{\delta_\theta}\right] \propto \left[\frac{V_\theta}{\delta_\theta^2}\right] \propto \left[\frac{R_{v\theta}Sc}{\delta_\theta}\right] \propto [D_\theta]\,, \tag{B 12a}$$

$$\left[\frac{dR_{u\theta}}{dt}\right] \propto \left[\frac{R_{u\theta}}{\delta_\theta}\frac{d\delta_\theta}{dt}\right] \propto [\Pi_{u\theta}] \propto \left[\frac{R_{v\theta}U_s}{\delta}\right] \propto \left[\frac{R_sSc}{\delta_\theta}\right] \propto \left[\frac{Tt_{u\theta}}{\delta_\theta}\right] \propto \left[\frac{M_{u\theta}}{\delta_\theta}\right] \propto \left[\frac{R_{u\theta}}{\delta_\theta^2}\right] \propto [D_{u\theta}] \tag{B 12b}$$

$$\left[\frac{dR_{v\theta}}{dt}\right] \propto \left[\frac{R_{v\theta}}{\delta_\theta}\frac{d\delta_\theta}{dt}\right] \propto [\Pi_{v\theta}] \propto \left[\frac{Pt_{v\theta}}{\delta_\theta}\right] \propto \left[\frac{K_vSc}{\delta_\theta}\right] \propto \left[\frac{Tt_{v\theta}}{\delta_\theta}\right] \propto \left[\frac{M_{v\theta}}{\delta_\theta}\right] \propto \left[\frac{R_{v\theta}}{\delta_\theta^2}\right] \propto [D_{v\theta}] \tag{B 12c}$$

The first term in equation (B 12*a*) is included to allow for the general possibility that the scale for the scalar variance is a function of time. If this is not the case (as in this first scalar geometry being considered), the term is zero and consequently does not appear in the equation or provide a constraint for the similarity analysis.

The proportionality of the second and fifth terms in equation (B 12*a*) imply that

$$V_\theta \propto (Sc)^2 \propto (U_d\Theta)^2\,. \tag{B 13}$$

Thus, the similarity scale for the scalar variance is independent of time in this two-stream geometry. As noted above, in this case the first constraint in equation (B 12*a*) would not appear because this term is zero in the original equation. The scales for the other moments in the scalar variance equation are given in table 2.

The proportionality of the second and fifth terms in equation (B 12*c*) results in

$$\left(\frac{d\delta_\theta}{dt}\right)^2 \propto U_s^2\,, \tag{B 14}$$

or

$$\frac{1}{\delta_\theta^2} \propto \frac{1}{\delta^2}\,, \tag{B 15}$$

implying

$$(t-t_{o\theta})^{-1} \propto (t-t_o)^{-1}\,, \tag{B 16}$$

Term	Form	Similarity Conditions
$\Theta - \Theta_1$	$Sc(t)sc(\eta_\theta)$	$Sc \propto U_d\Theta$ or $\frac{1}{\delta_\theta}$
$\overline{\theta^2}$	$V_\theta(t)v_\theta(\eta_\theta)$	$V_\theta \propto Sc^2$
$\overline{u\theta}$	$R_{u\theta}(t)r_{u\theta}(\eta_\theta)$	$R_{u\theta} \propto Sc\frac{d\delta_\theta}{dt}$
$\overline{v\theta}$	$R_{v\theta}(t)r_{v\theta}(\eta_\theta)$	$R_{v\theta} \propto Sc\frac{d\delta_\theta}{dt}$
$\overline{\frac{p}{\rho}\frac{\partial\theta}{\partial x}}$	$\Pi_{u\theta}(t)\pi_{u\theta}(\eta_\theta)$	$\Pi_{u\theta} \propto \frac{Sc}{\delta_\theta^2}\frac{d\delta_\theta}{dt}$
$\overline{\frac{p}{\rho}\frac{\partial\theta}{\partial y}}$	$\Pi_{v\theta}(t)\pi_{v\theta}(\eta_\theta)$	$\Pi_{v\theta} \propto \frac{Sc}{\delta_\theta^2}\frac{d\delta_\theta}{dt}$
$\overline{v\theta^2}$	$Tt_\theta(t)tt_\theta(\eta_\theta)$	$Tt_\theta \propto Sc^2\frac{d\delta_\theta}{dt}$
$\overline{uv\theta}$	$Tt_{u\theta}(t)tt_{u\theta}(\eta_\theta)$	$Tt_{u\theta} \propto \frac{Sc}{\delta_\theta}\frac{d\delta_\theta}{dt}$
$\overline{v^2\theta}$	$Tt_{v\theta}(t)tt_{v\theta}(\eta_\theta)$	$Tt_{v\theta} \propto \frac{Sc}{\delta_\theta}\frac{d\delta_\theta}{dt}$
$\overline{\frac{p\theta}{\rho}}$	$Pt_{v\theta}(t)pt_{v\theta}(\eta_\theta)$	$Pt_{v\theta} \propto \frac{Sc}{\delta_\theta}\frac{d\delta_\theta}{dt}$
$\overline{u\frac{\partial\theta}{\partial y}}$	$M_{u\theta}(t)m_{u\theta}(\eta_\theta)$	$M_{u\theta} \propto \frac{Sc}{\delta_\theta}\frac{d\delta_\theta}{dt}$
$\overline{v\frac{\partial\theta}{\partial y}}$	$M_{v\theta}(t)m_{v\theta}(\eta_\theta)$	$M_{v\theta} \propto \frac{Sc}{\delta_\theta}\frac{d\delta_\theta}{dt}$
ϵ_θ	$D_\theta(t)d_\theta(\eta_\theta)$	$D_\theta \propto \frac{Sc^2}{\delta_\theta}\frac{d\delta_\theta}{dt}$
$\epsilon_{u\theta}$	$D_{u\theta}(t)d_{u\theta}(\eta_\theta)$	$D_{u\theta} \propto \frac{Sc}{\delta_\theta^2}\frac{d\delta_\theta}{dt}$
$\epsilon_{v\theta}$	$D_{v\theta}(t)d_{v\theta}(\eta_\theta)$	$D_{v\theta} \propto \frac{Sc}{\delta_\theta^2}\frac{d\delta_\theta}{dt}$

TABLE 2. Similarity forms for terms in the scalar equations

where t_o is the location of the virtual origin for the velocity field and $t_{o\theta}$ is the virtual origin for the scalar field. This condition can also be written as

$$\frac{(t - t_{o\theta})}{(t - t_o)} = \text{constant}\,, \tag{B 17}$$

from which it is clear that a similarity solution can only exist for the equations governing the scalar field if the virtual origin of the scalar field is located at the same point as the

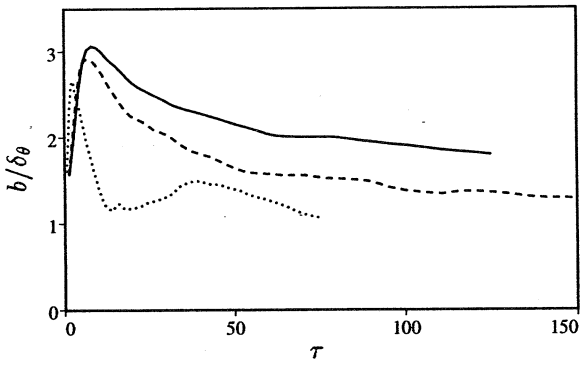

FIGURE 16. Hydrodynamic to scalar width ratio for the ——— unforced, ---- weakly forced, and ····· strongly forced wake simulations.

virtual origin of the velocity field. Note that this condition can also be derived from the proportionality of the fourth and fifth terms in equation (B 12*c*).

Although not needed to close the mean scalar equation, the streamwise scalar flux $\overline{u\theta}$ is also nonzero in this flow as a result of the mean shear. The terms in this equation provide no additional constraints on the self-similar solution; their form is also given in table 2.

In all three wake flows, the evolution of a passive scalar field of the type discussed above (ranging from zero to one in the two free streams) has been calculated along with the hydrodynamic flow field. Although the terms in the equations governing the second-order moments of the scalar statistics have not been examined, the behavior of the mean scalar field, the scalar fluctuation intensity, and both components of the scalar flux have been studied for the unforced case. All of these quantities appear to be evolving self-similarly over the self-similar period of the hydrodynamic evolution as evidenced by reasonable collapse of the profiles when scaled by the appropriate variables. Although the length scale b does a fair job of collapsing profiles from different times, better collapse is obtained by scaling with a scalar thickness δ_θ derived from the mean scalar profile. Here δ_θ is taken to be the distance between the points where $\Theta = 0.25$ and $\Theta = 0.75$. Figure 16 contains the time evolution of the ratio b/δ_θ. For all cases this ratio is approximately constant over the self-similar periods defined previously, as required for self-similarity from equation (B 15). Note that the ratio between δ_θ of an error function and b of its derivative (a gaussian) is given by $b/\delta_\theta = 1.75$, which lies between the unforced and weakly forced cases in figure 16.

The analysis of the scalar field in a temporally evolving plane wake flow can easily be extended to a second geometry in which there is a scalar deficit or surplus in the wake. The analysis for all of the higher-order moments is the same as the analysis for the previous geometry. The only difference between the two problems is that the scale for the mean value of the scalar differs. Thus, all that is necessary to extend the analysis to this second geometry is an analysis of the equation for the mean value of the scalar. When a scalar deficit occurs in the wake it is conventional to write the equation in a deficit form; *i.e.*,

$$\frac{\partial(\Theta_\infty - \Theta)}{\partial t} = \frac{\partial \overline{v\theta}}{\partial y} + \alpha \frac{\partial^2(\Theta_\infty - \Theta)}{\partial y^2} \tag{B 18}$$

where Θ_∞ is the value of the scalar in the free stream. This equation can be integrated

to yield

$$\frac{\partial}{\partial t}\int_{-\infty}^{\infty}(\Theta_\infty - \Theta)\,dy = 0 \tag{B 19}$$

if it is assumed that there is no free-stream turbulence and the effect of the diffusion goes to zero as $y \to \pm\infty$.

Thus, if it is hypothesized that a similarity solutions of the form

$$\Theta_\infty - \Theta = Sc(t)sc(\eta_\theta) \tag{B 20}$$

and

$$\overline{v\theta} = R_{v\theta}(t)r_{v\theta}(\eta_\theta) \tag{B 21}$$

exists for the present geometry, it follows that these solutions are consistent with the equations for the mean scalar if

$$Sc\delta_\theta \propto \text{constant} \tag{B 22a}$$

$$\left[\frac{dSc}{dt}\right] \propto \left[\frac{Sc}{\delta_\theta}\frac{d\delta_\theta}{dt}\right] \propto \left[\frac{R_{v\theta}}{\delta_\theta}\right] \propto \left[\frac{Sc}{\delta_\theta^2}\right] \tag{B 22b}$$

Thus, for the deficit flow

$$Sc \propto \frac{1}{\delta_\theta} \tag{B 23a}$$

$$\frac{d\delta_\theta^2}{dt} \propto \text{constant}\,, \tag{B 23b}$$

which is analogous to the conditions derived for the velocity field. The scale for all of the higher-order moments can also be deduced from the analysis of the equations outlined above, but using the new scale Sc for the mean scalar field.

References

ANTONIA, R. A., BROWNE, L. W. B. & BISSET, D. K. 1987 A description of the organized motion in the turbulent far wake of a cylinder at low reynolds number. *J. Fluid Mech.* **184**, 423–444.

BROWAND, F. K. & TROUTT, T. R. 1980 A note on spanwise structure in the two-dimensional mixing layer. *J. Fluid Mech.* **97**, 771–781.

GEORGE, W. K. 1989 The self-preservation of turbulent flows and its relation to initial conditions and coherent structure. In *Advances in Turbulence* (ed. W. K. George & R. Arndt), pp. 39–73. Hemisphere.

GEORGE, W. K. 1994 Some new ideas for similarity of turbulent shear flows. In *Proc. of the Int. Symp. on Turbulent Heat and Mass Transfer*, Lisbon Portugal.

GHOSAL, S. & ROGERS, M. M. 1996 A numerical study of self-similarity in a turbulent plane wake using large eddy simulation. In preparation.

HAYAKAWA, M. & HUSSAIN, F. 1989 Three-dimensionality of organized structures in a plane wake. *J. Fluid Mech.* **206**, 375–404.

LASHERAS, J. C. & MEIBURG, E. 1990 Three-dimensional vorticity modes in the wake of a flat plate. *Phys. of Fluids* **2**, 371–380.

MARASLI, B., CHAMPAGNE, F. H. & WYGNANSKI, I. 1992 Effect of travelling waves on the growth of a plane turbulent wake. *J. Fluid Mech.* **235**, 511–528.

ROGERS, M. M. & MOIN, P. 1987 The structure of the vorticity field in homogeneous turbulent flows. *J. Fluid Mech.* **176**, 33–66.

ROGERS, M. M. & MOSER, R. D. 1993 The three-dimensional evolution of a plane mixing layer: the kelvin-helmholtz rollup. *J. Fluid. Mech.* **243**, 183–226.

ROGERS, M. M. & MOSER, R. D. 1994 Direct simulation of a self-similar turbulent mixing layer. *Phys. Fluids* **6**, 903–923.

SPALART, P. R. 1988 Direct simulation of a turbulent boundary layer up to $r_\theta = 1410$. *J. Fluid Mech.* **187**, 61–98.

SPALART, P. R., MOSER, R. D. & ROGERS, M. M. 1991 Spectral methods for the navier–stokes equations with one infinite and two periodic directions. *J. Comp. Phys.* **96**, 297–324.

TENNEKES, H. & LUMLEY, J. L. 1972 *A First Course in Turbulence.* MIT Press.

TOWNSEND, A. A. 1976 *Structure of Turbulent Shear Flow.* Cambridge University Press.

WEYGANDT, J. H. & MEHTA, R. D. 1993 Three-dimensional structure of straight and curved plane wakes. JIAA TR-110, Stanford University.

WYGNANSKI, I., CHAMPAGNE, F. & MARASLI, B. 1986 On the large-scale structures in two-dimensional small-deficit, turbulent wakes. *J. Fluid Mech.* **168**, 31–71.

List of Recent TAM Reports

No.	Authors	Title	Date
742	Weaver, R. L., and W. Sachse	Diffusion of ultrasound in a glass bead slurry—*Journal of the Acoustical Society of America* **97**, 2094–2102 (1995)	Dec. 1993
743	Sundermeyer, J. N., and R. L. Weaver	On crack identification and characterization in a beam by nonlinear vibration analysis—*Journal of Sound and Vibration* **183**, 857–872 (1995)	Dec. 1993
744	Li, L., and N. R. Sottos	Predictions of static displacements in 1–3 piezocomposites—*Journal of Intelligent Materials Systems and Structures* **6**, 169–180 (1995)	Dec. 1993
745	Jones, S. W.	Chaotic advection and dispersion—*Physica D* **76**, 55–69 (1994)	Jan. 1994
746	Stewart, D. S., and J. Yao	Critical detonation shock curvature and failure dynamics: Developments in the theory of detonation shock dynamics—*Developments in Theoretical and Applied Mechanics* **17** (1994)	Feb. 1994
747	Mei, R., and R. J. Adrian	Effect of Reynolds-number-dependent turbulence structure on the dispersion of fluid and particles—*Journal of Fluids Engineering* **117**, 402-409 (1995)	Feb. 1994
748	Liu, Z.-C., R. J. Adrian, and T. J. Hanratty	Reynolds-number similarity of orthogonal decomposition of the outer layer of turbulent wall flow—*Physics of Fluids* **6**, 2815–2819 (1994)	Feb. 1994
749	Barnhart, D. H., R. J. Adrian, and G. C. Papen	Phase-conjugate holographic system for high-resolution particle image velocimetry—*Applied Optics* **33**, 7159–7170 (1994)	Feb. 1994
750	Qi, Q., W. D. O'Brien Jr., and J. G. Harris	The propagation of ultrasonic waves through a bubbly liquid into tissue: A linear analysis—*IEEE Transactions on Ultrasonics, Ferroelectrics and Frequency Control* **42**, 28–36 (1995)	Mar. 1994
751	Mittal, R., and S. Balachandar	Direct numerical simulation of flow past elliptic cylinders—*Journal of Computational Mechanics*, in press (1996)	May 1994
752	Students in TAM 293–294	Thirty-first student symposium on engineering mechanics, J. W. Phillips, coordinator: Selected senior projects by D. N. Anderson, J. R. Dahlen, M. J. Danyluk, A. M. Dreyer, K. M. Durkin, J. J. Kriegsmann, J. T. McGonigle, and V. Tyagi	May 1994
753	Thoroddsen, S. T.	The failure of the Kolmogorov refined similarity hypothesis in fluid turbulence—*Physics of Fluids* **7**, 691–693 (1995)	May 1994
754	Turner, J. A., and R. L. Weaver	Time dependence of multiply scattered diffuse ultrasound in polycrystalline media—*Journal of the Acoustical Society of America* **97**, 2639–2644 (1995)	June 1994
755	Riahi, D. N.	Finite-amplitude thermal convection with spatially modulated boundary temperatures—*Proceedings of the Royal Society of London A* **449**, 459–478 (1995)	June 1994
756	Riahi, D. N.	Renormalization group analysis for stratified turbulence—*International Journal of Mathematics and Mathematical Sciences*, in press (1996)	June 1994
757	Riahi, D. N.	Wave-packet convection in a porous layer with boundary imperfections—*Journal of Fluid Mechanics* **318**, 107-128 (1996)	June 1994
758	Jog, C. S., and R. B. Haber	Stability of finite element models for distributed-parameter optimization and topology design—*Computer Methods in Applied Mechanics and Engineering*, in press (1996).	July 1994
759	Qi, Q., and G. J. Brereton	Mechanisms of removal of micron-sized particles by high-frequency ultrasonic waves—*IEEE Transactions on Ultrasonics, Ferroelectrics and Frequency Control* **42**, 619–629 (1995)	July 1994
760	Shawki, T. G.	On shear flow localization with traction-controlled boundaries—*International Journal of Solids and Structures* **32**, 2751–2778 (1995)	July 1994
761	Balachandar, S., D. A. Yuen, and D. M. Reuteler	High Rayleigh number convection at infinite Prandtl number with temperature-dependent viscosity	July 1994
762	Phillips, J. W.	Arthur Newell Talbot—Proceedings of a conference to honor TAM's first department head and his family	Aug. 1994

List of Recent TAM Reports (cont'd)

No.	Authors	Title	Date
763	Man., C. S., and D. E. Carlson	On the traction problem of dead loading in linear elasticity with initial stress—*Archive for Rational Mechanics and Analysis* **128**, 223–247 (1994)	Aug. 1994
764	Zhang, Y., and R. L. Weaver	Leaky Rayleigh wave scattering from elastic media with random microstructures—*Journal of the Acoustical Society of America* **99**, 88-99 (1996)	Aug. 1994
765	Cortese, T. A., and S. Balachandar	High-performance spectral simulation of turbulent flows in massively parallel machines with distributed memory—*International Journal of Supercomputer Applications* **9**, 185–202 (1995)	Aug. 1994
766	Balachandar, S.	Signature of the transition zone in the tomographic results extracted through the eigenfunctions of the two-point correlation—*Geophysical Research Letters* **22**, 1941–1944 (1995)	Sept. 1994
767	Piomelli, U.	Large-eddy simulation of turbulent flows	Sept. 1994
768	Harris, J. G., D. A. Rebinsky, and G. R. Wickham	An integrated model of scattering from an imperfect interface—*Journal of the Acoustical Society of America* **99**, 1315-1325 (1996)	Sept. 1994
769	Hsia, K. J., and Z.-Q. Xu	The mathematical framework and an approximate solution of surface crack propagation under hydraulic pressure loading—*International Journal of Fracture*, in press (1996)	Sept. 1994
770	Balachandar, S.	Two-point correlation and its eigen-decomposition for optimal characterization of mantle convection	Oct. 1994
771	Lufrano, J. M., and P. Sofronis	Numerical analysis of the interaction of solute hydrogen atoms with the stress field of a crack—*International Journal of Solids and Structures*, in press (1996)	Oct. 1994
772	Aref, H., and S. W. Jones	Motion of a solid body through ideal fluid—Proceedings of the DCAMM 25th Anniversary Volume, 55-68 (1994)	Oct. 1994
773	Stewart, D. S., T. D. Aslam, J. Yao, and J. B. Bdzil	Level-set techniques applied to unsteady detonation propagation—In "Modeling in Combustion Science," *Lecture Notes in Physics* (1995)	Oct. 1994
774	Mittal, R., and S. Balachandar	Effect of three-dimensionality on the lift and drag of circular and elliptic cylinders—*Physics of Fluids* **7**, 1841–1865 (1995)	Oct. 1994
775	Stewart, D. S., T. D. Aslam, and J. Yao	On the evolution of cellular detonation	Nov. 1994 *Revised* Jan. 1996
776	Aref, H.	On the equilibrium and stability of a row of point vortices—*Journal of Fluid Mechanics* **290**, 167–181 (1995)	Nov. 1994
777	Cherukuri, H. P., T. G. Shawki, and M. El-Raheb	An accurate finite-difference scheme for elastic wave propagation in a circular disk—*Journal of the Acoustical Society of America*, in press (1996)	Nov. 1994
778	Li, L., and N. R. Sottos	Improving hydrostatic performance of 1–3 piezocomposites—*Journal of Applied Physics* **77**, 4595–4603 (1995)	Dec. 1994
779	Phillips, J. W., D. L. de Camara, M. D. Lockwood, and W. C. C. Grebner	Strength of silicone breast implants—*Plastic and Reconstructive Surgery* **97**, 1215-1225 (1996)	Jan. 1995
780	Xin, Y.-B., K. J. Hsia, and D. A. Lange	Quantitative characterization of the fracture surface of silicon single crystals by confocal microscopy—*Journal of the American Ceramics Society* **78**, 3201-3208 (1995)	Jan. 1995
781	Yao, J., and D. S. Stewart	On the dynamics of multi-dimensional detonation—*Journal of Fluid Mechanics* **309**, 225-275 (1996)	Jan. 1995
782	Riahi, D. N., and T. L. Sayre	Effect of rotation on the structure of a convecting mushy layer—*Acta Mechanica*, in press (1996)	Feb. 1995
783	Batchelor, G. K., and TAM faculty and students	A conversation with Professor George K. Batchelor	Feb. 1995

List of Recent TAM Reports (cont'd)

No.	Authors	Title	Date
784	Sayre, T. L., and D. N. Riahi	Effect of rotation on flow instabilities during solidification of a binary alloy—*International Journal of Engineering Science,* in press (1996)	Feb. 1995
785	Xin, Y.-B., and K. J. Hsia	A technique to generate straight surface cracks for studying the dislocation nucleation condition in brittle materials —*Acta Metallurgica et Materialia* **44**, 845-853 (1996).	Mar. 1995
786	Riahi, D. N.	Finite bandwidth, long wavelength convection with boundary imperfections: Near-resonant wavelength excitation—*International Journal of Mathematics and Mathematical Sciences,* in press (1996)	Mar. 1995
787	Turner, J. A., and R. L. Weaver	Average response of an infinite plate on a random foundation—*Journal of the Acoustical Society of America* **99**, 2167-2175 (1996)	Mar. 1995
788	Weaver, R. L., and D. Sornette	The range of spectral correlations in pseudointegrable systems: GOE statistics in a rectangular membrane with a point scatterer—*Physical Review E* **52**, 341 (1995)	Apr. 1995
789	Students in TAM 293–294	Thirty-second student symposium on engineering mechanics, J. W. Phillips, coordinator: Selected senior projects by K. F. Anderson, M. B. Bishop, B. C. Case, S. R. McFarlin, J. M. Nowakowski, D. W. Peterson, C. V. Robertson, and C. E. Tsoukatos	Apr. 1995
790	Figa, J., and C. J. Lawrence	Linear stability analysis of a gravity-driven Newtonian coating flow on a planar incline	May 1995
791	Figa, J., and C. J. Lawrence	Linear stability analysis of a gravity-driven viscosity-stratified Newtonian coating flow on a planar incline	May 1995
792	Cherukuri, H. P., and T. G. Shawki	On shear band nucleation and the finite propagation speed of thermal disturbances—*International Journal of Solids and Structures,* in press (1996)	May 1995
793	Harris, J. G.	Modeling scanned acoustic imaging of defects at solid interfaces—Chapter in *IMA Workshop on Inverse Problems in Wave Propagation,* Springer-Verlag, in press (1996)	May 1995
794	Sottos, N. R., J. M. Ockers, and M. J. Swindeman	Thermoelastic properties of plain weave composites for multilayer circuit board applications	May 1995
795	Aref, H., and M. A. Stremler	On the motion of three point vortices in a periodic strip—*Journal of Fluid Mechanics* **314**, 1-25 (1996)	June 1995
796	Barenblatt, G. I., and N. Goldenfeld	Does fully-developed turbulence exist? Reynolds number independence versus asymptotic covariance—*Physics of Fluids* **7**, 3078–3082 (1995)	June 1995
797	Aslam, T. D., J. B. Bdzil, and D. S. Stewart	Level set methods applied to modeling detonation shock dynamics—*Journal of Computational Physics,* in press (1996)	June 1995
798	Nimmagadda, P. B. R., and P. Sofronis	The effect of interface slip and diffusion on the creep strength of fiber and particulate composite materials—*Mechanics of Materials,* in press (1996)	July 1995
799	Hsia, K. J., T.-L. Zhang, and D. F. Socie	Effect of crack surface morphology on the fracture behavior under mixed mode loading —*ASTM Special Technical Publication* 1296, in press (1996)	July 1995
800	Adrian, R. J.	Stochastic estimation of the structure of turbulent fields	Aug. 1995
801	Riahi, D. N.	Perturbation analysis and modeling for stratified turbulence	Aug. 1995
802	Thoroddsen, S. T.	Conditional sampling of dissipation in high Reynolds number turbulence—*Physics of Fluids* **8**, 1333-1335	Aug. 1995
803	Riahi, D. N.	On the structure of an unsteady convecting mushy layer	Aug. 1995
804	Meleshko, V. V.	Equilibrium of an elastic rectangle: The Mathieu–Inglis–Pickett solution revisited—*Journal of Elasticity* **40**, 207-238 (1995)	Aug. 1995
805	Jonnalagadda, K., G. E. Kline, and N. R. Sottos	Local displacements and load transfer in shape memory alloy composites	Aug. 1995

List of Recent TAM Reports (cont'd)

No.	Authors	Title	Date
806	Nimmagadda, P. B. R., and P. Sofronis	On the calculation of the matrix–reinforcement interface diffusion coefficient in composite materials at high temperatures—*Acta Metallurgica et Materialia*, in press (1996)	Aug. 1995
807	Carlson, D. E., and D. A. Tortorelli	On hyperelasticity with internal constraints—*Journal of Elasticity* **42**, 91-98 (1966)	Aug. 1995
808	Sayre, T. L., and D. N. Riahi	Oscillatory instabilities of the liquid and mushy layers during solidification of alloys under rotational constraint—*Acta Mechanica*, in press (1996)	Sept. 1995
809	Xin, Y.-B., and K. J. Hsia	Simulation of the brittle-ductile transition in silicon single crystals using dislocation mechanics	Oct. 1995
810	Ulysse, P., and R. E. Johnson	A plane-strain upper-bound analysis of unsymmetrical single-hole and multi-hole extrusion processes	Oct. 1995
811	Fried, E.	Continua described by a microstructural field—*Zeitschrift für angewandte Mathematik und Physik*, in press (1996)	Nov. 1995
812	Mittal, R., and S. Balachandar	Autogeneration of three-dimensional vortical structures in the near wake of a circular cylinder	Nov. 1995
813	Segev, R., E. Fried, and G. de Botton	Force theory for multiphase bodies—*Journal of Geometry and Physics*, in press (1996)	Dec. 1995
814	Weaver, R. L.	The effect of an undamped finite-degree-of-freedom "fuzzy" substructure: Numerical solutions and theoretical discussion	Jan. 1996
815	Haber, R. B., C. S. Jog, and M. P. Bensøe	A new approach to variable-topology shape design using a constraint on perimeter—*Structural Optimization* **11**, 1-12 (1996)	Feb. 1996
816	Xu, Z.-Q., and K. J. Hsia	A numerical solution of a surface crack under cyclic hydraulic pressure loading	Mar. 1996
817	Adrian, R. J.	Bibliography of particle velocimetry using imaging methods: 1917–1995—*Produced and distributed in cooperation with TSI, Inc., St. Paul, Minn.*	Mar. 1996
818	Fried, E., and G. Grach	An order-parameter based theory as a regularization of a sharp-interface theory for solid–solid phase transitions—*Archive for Rational Mechanics and Analysis*, in press (1996)	Mar. 1996
819	Vonderwell, M. P., and D. N. Riahi	Resonant instability mode triads in the compressible boundary-layer flow over a swept wing	Mar. 1996
820	Short, M., and D. S. Stewart	Low-frequency two-dimensional linear instability of plane detonation	Mar. 1996
821	Casagranda, A., and P. Sofronis	On the scaling laws for the consolidation of nanocrystalline powder compacts	Apr. 1996
822	Xu, S., and D. S. Stewart	Deflagration-to-detonation transition in porous energetic materials: A comparative model study	Apr. 1996
823	Weaver, R. L.	Mean and mean-square responses of a prototypical master/fuzzy structure	Apr. 1996
824	Fried, E.	Correspondence between a phase-field theory and a sharp-interface theory for crystal growth	Apr. 1996
825	Students in TAM 293–294	Thirty-third student symposium on engineering mechanics, J. W. Phillips, coordinator: Selected senior projects by W. J. Fortino II, A. A. Mordock, and M. R. Sawicki	May 1995
826	Riahi, D. N.	Effects of roughness on nonlinear stationary vortices in rotating disk flows	June 1996
827	Riahi, D. N.	Nonlinear instabilities of shear flows over rough walls	June 1996
828	Weaver, R. L.	Multiple scattering theory for a plate with sprung masses: Mean and mean-square responses	July 1996
829	Moser, R. D., M. M. Rogers, and D. W. Ewing	Self-similarity of time-evolving plane wakes	July 1996